Ultralow thermal conductivity in diamondoid lattices: high thermoelectric performance in chalcopyrite Cu0.8+yAg0.2In1-yTe2

Journal:	*Energy & Environmental Science*
Manuscript ID	EE-ART-07-2020-002323.R2
Article Type:	Paper
Date Submitted by the Author:	07-Sep-2020
Complete List of Authors:	Xie, Hongyao; Northwestern University Hao, Shiqiang; Northwestern University, Materials Science Cai, Songting; Northwestern University, Material Science and Engineering Bailey, Trevor; University of Michigan, Department of Physics Uher, Ctirad; University of Michigan, Department of Physics Wolverton, Chris; Northwestern University, Department of Materials Science and Engineering Dravid, Vinayak; Northwestern University, Materials Science & Engineering Kanatzidis, Mercouri; Northwestern University, Department of Chemistry

The most efficient thermoelectric materials require extremely low thermal conductivity. For some time, compounds with diamond-like structures have been considered unsuitable for thermoelectric applications. Because the very high thermal conductivity of such compounds mimicking diamond. However, there are intriguing notable exceptions to this such as $AgInTe_2$ which unlike its close relative $CuInTe_2$, exhibits an unusually low thermal conductivity, of ~1.5 $Wm^{-1}K^{-1}$ at 300 K. The essential nature of the different heat transport properties between $AgInTe_2$ and $CuInTe_2$ is unclear and we performed an in-depth fundamental study to understand the origin. We found the weak Ag-Te bonding in $AgInTe_2$ would lead to a strong interaction between low frequency optical phonons and heat carrying acoustic phonons, which greatly diminishes the phonon relaxation times, thus, leads to the low thermal conductivity of $AgInTe_2$. Moreover, we demonstrate a great improvement in thermoelectric performance by Ag alloying and composition control in $Cu_{0.8+y}Ag_{0.2}In_{1-y}Te_2$. An ultralow thermal conductivity of 0.36 $Wm^{-1}K^{-1}$ and a $ZT_{\max}$ of ~ 1.6 is achieved at 850 K for $Cu_{0.89}Ag_{0.2}In_{0.91}Te$. This work clarifies the significant role of phonon coupling effects in the low thermal conductivity of $AgInTe_2$, and assists in formulating conceptual strategies for further optimizing the thermoelectric performance of other diamond-like materials.

Ultralow thermal conductivity in diamondoid lattices: high thermoelectric performance in chalcopyrite $Cu_{0.8+y}Ag_{0.2}In_{1-y}Te_2$

Hongyao Xie[1], Shiqiang Hao[2], Songting Cai[2], Trevor P. Bailey[3], Ctirad Uher[3], Christopher Wolverton[2], Vinayak P. Dravid[2], and Mercouri G. Kanatzidis[1*]

[1]Department of Chemistry, Northwestern University, Evanston, Illinois 60208, USA.
[2]Department of Materials Science and Engineering, Northwestern University, Evanston, Illinois 60208, USA.
[3]Department of Physics, University of Michigan, Ann Arbor, Michigan 48109, USA.

Abstract: Because of its unique transport properties, $CuInTe_2$ has been considered as a promising p-type material for thermoelectric applications. However, its diamondoid structure gives it a high intrinsic lattice thermal conductivity that greatly limits its thermoelectric performance. In this study, we demonstrate that Ag alloying gives rise to an extremely low lattice thermal conductivity of 0.47 $Wm^{-1}K^{-1}$ for $Cu_{0.8}Ag_{0.2}InTe_2$ at 850 K. Moreover, we found Cu doping significantly improves the carrier mobility while simultaneously increasing the carrier concentration. As a result, the power factor of $Cu_{0.8}Ag_{0.2}InTe_2$ increases and a maximum *ZT* of ~ 1.6 is achieved at 850 K. Both DFT calculations and low temperature heat capacity measurements suggest a strong interaction between low frequency optical phonons and heat carrying acoustic phonons, which is derived from the weak Ag-Te bonding. This strong phonon coupling decreases the Debye temperature and induces a low sound velocity.

Keyword: diamond-like structure, acceptor level, phonon-phonon coupling, thermal conductivity

1. Introduction

In order to realize the large-scale commercial application of thermoelectric conversion technology for power generation, high-performance thermoelectric materials are required. [1-3] The performance of a thermoelectric material is evaluated by the dimensionless figure of merit: $ZT=S^2\sigma T/\kappa$. Obviously, a high-performance thermoelectric material requires a large Seebeck coefficient S, a high electrical conductivity σ, as well as a low thermal conductivity κ.[4-7] Many powerful concepts, such as band convergence,[8-10] energy filtering,[11, 12] nanostructuring[13-16] and discordant atoms[17-21] have been developed to improve existing thermoelectric materials, but great progress has also been made in identifying novel efficient thermoelectric compounds.[22-26] Most of the state-of-art thermoelectric materials have been narrow band gap semiconductors, such as Bi_2Te_3,[27-31] PbTe,[32-35] SnSe,[10, 22] $CoSb_3$[36-39] and GeTe,[40-44] to name but a few. In contrast, the wide band gap ($E_g \geq 1$ eV) thermoelectric materials have received limited attention, since they usually are poor conductors. Recently, $ZT>1$, a benchmark of thermoelectric performance, has been reported in a series of wide band gap diamond-like compounds: $CuInTe_2$,[45-49] $CuGaTe_2$[50-52] and $AgGaTe_2$[53, 54]. These studies have sparked intense interest in exploring the thermoelectric properties of diamond-like materials.

The ternary I-III-VI_2 type materials (I = Cu, Ag; III = Ga, In; VI = S, Se, Te) are a big family of wide band gap semiconductors, which possess various unique electronic and heat transport properties.[55] These materials possess the tetragonal chalcopyrite structure with space group $I\text{-}42d$,[56] which is essentially a double zinc-blende cell. Among them, $CuInTe_2$ was reported with a ZT of 1.18 at 850 K[45]. $CuInTe_2$ is a p-type semiconductor with an electronic energy band gap about 1.0 eV.[57] Despite the relatively wide band gap, pristine $CuInTe_2$ exhibits a decent electrical conductivity ~20 S cm^{-1} and a high Seebeck coefficient of ~410 μVK^{-1} at room temperature, owing to its considerable carrier concentration of ~10^{18} cm^{-3}.[46] Many efforts have been carried out to improve its thermoelectric performance, such as elemental doping,[46] forming solid solutions[47] and introducing nanostructures[58]. However, because of the diamond derived crystal structure, the intrinsic lattice thermal conductivity of $CuInTe_2$ is high as ~6.1 $Wm^{-1}K^{-1}$ at room temperature,[45] which restricts its thermoelectric performance.

In contrast, despite the identical diamond-like crystal structure (**Figure 1**), $AgInTe_2$ exhibits an unusually low intrinsic lattice thermal conductivity, of ~1.5 $Wm^{-1}K^{-1}$ at room temperature[59]. Previous studies have demonstrated that $AgInTe_2$ alloying is an effective approach to suppress the lattice thermal conductivity of $CuInTe_2$, and an extremely low lattice thermal conductivity of ~0.3 $Wm^{-1}K^{-1}$ was obtained in the $Cu_{0.75}Ag_{0.2}InTe_2$ compound at 886 K.[47] However, the inferior electrical conductivity of $AgInTe_2$ also degrades the power factor ($S^2\sigma$) of the compound, and the *ZT* value was not actually improved.

Moreover, although Ag alloying appears as an effective way to reduce the lattice thermal conductivity of $CuInTe_2$, the essential nature of the different heat transport properties between $AgInTe_2$ and $CuInTe_2$ is still unclear. In fact, the huge difference in lattice thermal conductivity has also been observed between $CuGaTe_2$[52] and $AgGaTe_2$[54]. Although the atomic mass difference between Cu and Ag is part of the reason for the thermal conductivity disparity, it is insufficient on its own to account for such a large drop. Hence, in order to optimize the thermoelectric performance of these compounds, it is important to understand first the underlying mechanism for the low thermal conductivity in Ag-based diamond-like compounds.

To this end, we synthesized a series of $Cu_{1-x}Ag_xInTe_2$ solid solutions by vacuum melting-annealing combined with spark plasma sintering (SPS), and investigated the role of Cu and Ag on the electronic and heat transport properties. We found that the pristine $AgInTe_2$ exhibits intrinsically low carrier concentration, which leads to the large deterioration in the electrical conductivity of the Ag-alloyed $Cu_{1-x}Ag_xInTe_2$ compounds. However, this Ag alloying is very effective in reducing the lattice thermal conductivity of $CuInTe_2$, and an extremely low lattice thermal conductivity of ~0.47 $Wm^{-1}K^{-1}$ is obtained in $Cu_{0.8}Ag_{0.2}InTe_2$ at 850 K. The experimental results and theoretical calculations suggest that the chemical bonds of Ag-Te are much weaker than the Cu-Te bonds in the diamond-like structure. The weak bonding leads to large atomic displacement parameters (ADPs) for the Ag atoms as well as low frequency optical phonons. The calculated phonon dispersions and low temperature heat capacity measurements show that the Ag induced low frequency optical phonons are strongly coupled with the heat carrying acoustic phonons, thereby decreasing the Debye temperature and the phonon velocity. Moreover, the interaction between optical phonons and acoustic phonons induces a strong phonon resonance scattering, which effectively decreases the phonon relaxation time. All these factors contribute to an ultralow lattice thermal conductivity of $AgInTe_2$, which is ~0.26 $Wm^{-1}K^{-1}$ at 850 K. Furthermore, we were able to simultaneously optimize the thermal conductivity and the power factor of the $Cu_{0.8}Ag_{0.2}InTe_2$ system *via* Ag alloying and additional Cu substitution on the In site. As a result, a maximum *ZT* of ~ 1.6 is attained at 850 K for the $Cu_{0.89}Ag_{0.2}In_{0.91}Te_2$ compound. This work clarifies the fundamental nature of the large difference in heat transport behavior between Cu-based and Ag-based diamond-like compounds. As such, it assists in formulating conceptual strategies for further optimizing the thermoelectric performance of the diamond-like materials.

2. Experimental

2.1. Synthesis: A series of compounds with nominal compositions of $Cu_{1-x}Ag_xInTe_2$ (x=0, 0.2, 0.4, 0.6, 0.8 and 1) and $Cu_{0.8+y}Ag_{0.2}In_{1-y}Te_2$ (y=0.01, 0.02, 0.03, 0.04, 0.05, 0.06, 0.07, 0.08, 0.09 and 0.1) were synthesized by vacuum melting-annealing combined with spark plasma sintering (SPS). High-purity Cu (shot, 99.99%), Ag (shot, 99.99%), In (pellet, 99.999%), and Te (shot, 99.999%) were weighed and mixed to obtain the desired composition according to the stoichiometric ratio, with the total amount of every sample being 5g. Then, the mixtures were sealed in evacuated quartz tubes (the inner diameter is 10 mm and the thickness of its walls is 1.5 mm) and slowly heated up to 1323 K at a heating rate of 100 K h^{-1}. After holding at this temperature for 24 h, the tubes were quenched in cold water to room temperature and subsequently annealed at 673 K for 72 h. The obtained ingots were crushed and hand ground into fine powder, and sintered *via* the SPS apparatus at 773 K under a pressure of 40 MPa in vacuum for 5 min to obtain densified bulk samples (φ16 × 3.5 mm).

2.2. Characterization: The powder X-ray diffraction analysis (XRD; Rigaku Miniflex, Cu Kα) was performed to determine the phase composition of the sintered samples. The scanning range of 2θ was 10 - 90 degrees, and the scan increment was 0.02 degrees. The lattice parameters of all samples were calculated by the Rietveld refinement method; TEM analyses was done with an aberration corrected JEOL ARM200F microscope operated at 200 kV. The electron-beam transmitted TEM specimens were prepared by hand grinding and polishing, followed with Ar-ion milling (3 kV for ~1 hour until a hole is formed, followed by ion cleaning with 0.3 kV for 1 hour) under low temperature (liquid nitrogen stage). The elemental analyses of the sintered samples were obtained by field emission scanning electron microscopy (FESEM; Hitachi SU8030) with energy dispersive spectroscopy (EDS; Oxford AZtec X-max 80 SDD EDS detector); The optical band gap was determined by ultraviolet-visible spectroscopy. The diffuse reflectance (R) data of all samples were measured at room temperature *via* a Shimadzu UV-3101 PC spectrometer. These data were converted to absorption (α) using the Kubelka-Munk equation: $\alpha/S = (1-R)^2/2R$, where S is the scattering coefficient.

2.3. Transport Property Measurements: The SPSed samples were cut and polished into regular shapes for transport property measurements, a 3 × 3 × 12 mm bar for electrical properties measurement and a 6 × 6 × 1.5 mm piece for thermal conductivity measurement. The high temperature electrical conductivity (σ) and the Seebeck coefficient (S) were simultaneously measured using a commercial apparatus (ZEM-3, Ulvac Riko, Inc.) under a He atmosphere from 300 to 850 K. The thermal conductivity was calculated by using the thermal diffusivity (D), heat capacity (C_p) and sample density (ρ) according to the relationship $\kappa = DC_p\rho$. The thermal diffusivity was measured in an Ar atmosphere by the laser flash diffusivity method (LFA 457; Netzsch). The heat capacity was calculated by the Dulong-Petit law, and the sample density was determined by measuring the mass and dimensions of the sample. The calculation details of the lattice thermal conductivity are discussed in the **Supporting Information**. The high-temperature (300-813 K) Hall coefficient (R_H) was measured by a home-made apparatus in an Ar atmosphere. The Hall resistance was monitored with a Linear Research AC resistance bridge (LR-700) operated at 17 Hz, and the data were taken under a reversible magnetic field of 0.5 T provided by an air-bore Oxford superconducting magnet. The charge carrier concentration (p_H) and the charge carrier mobility (μ_H) were calculated from $p_H=1/eR_H$ and $\mu_H=\sigma R_H$. The low temperature Hall measurement in the range 10-300 K was performed in a Physical Property Measurement System (PPMS-9: Quantum Design) with a five-probe sample configuration by sweeping the magnetic field between -1.0 and 1.0 T. We have also measured the low temperature (10-300 K) electrical conductivity and low temperature (2-300 K) heat capacity (C_p) with the aid of the PPMS-9. The room temperature longitudinal and transverse sound velocities were measured by ultrasonic pulse-echo method with an oscilloscope (TDS2022; Tektronix) and ultrasonic pulse receiver (Panametrics 5072PR).

2.4. Theoretical Calculations: We used density functional theory within the generalized gradient approximation to calculate the total energies and relaxed geometries.[60] Periodic boundary conditions and a plane-wave basis set were implemented in the Vienna ab initio simulation package.[61] In all energy calculations, we adopt the Perdew-Burke-Ernzerhof exchange correlation functional with projector augmented wave potentials.[62] The numerical convergence of the total energies was set to be 3 meV/atom using a basis set energy cutoff of 400 eV and dense k meshes corresponding to 4000 k points per reciprocal atom in the Brillouin zone. To calculate the electronic energy band gap for a given unit cell, the energy eigenvalues at each k point in the Brillouin zone were evaluated and the band gap values determined from the difference between the conduction-band minimum (CBM) and valence-band maximum (VBM).

For the atomic displacement parameter (ADP), which is characterized as the mean-square amplitude of vibration of an atom around its equilibrium position, we used ab initio molecular dynamics calculations with the NVT ensemble. The molecular dynamics were carried out using supercells containing 64 atoms for 10000 steps with 5 fs time steps.

In lattice dynamics calculations, we first obtained the equilibrium structures by minimizing residual forces. When an atom in a structure is displaced from its equilibrium position, the potential energy of a system can be expressed as a Taylor series expansion of atomic displacements.[63] We construct the force constant matrix within the quasi-harmonic approximation by using the finite displacement method on the basis of the potential energy expression.[64] By accounting for the masses of the system, the phonon dispersion, including vibrational frequencies and vibrational eigenvectors, can be determined by diagonalization of the dynamical matrix.

3. Results and Discussion

3.1. Phase Composition and Microstructural Characterization

The powder XRD patterns and lattice parameters for the SPS-sintered $Cu_{1-x}Ag_xInTe_2$ (x = 0, 0.2, 0.4, 0.6, 0.8 and 1) samples are shown in **Figure 2a and 2b**. The XRD patterns of all samples can be indexed to the chalcopyrite structure with *I*-42*d* space group, and the Bragg peak positions shift to lower angles with increasing Ag content because of the larger atomic radius of Ag compared to Cu. The lattice parameters increase linearly with increasing Ag content, consistent with Vegard's law and verifying the successful alloying of Ag into the Cu sites in the chalcopyrite structure. The back scattered electron image (BSEI) of the polished surface and elemental distribution maps of all samples were obtained by FESEM with the aid of EDS. With similarly homogeneous distributions in all samples, here $Cu_{0.8}Ag_{0.2}InTe_2$ is selected as an example and shown in **Figure 2c**. The rest of the data are shown in **Figure S1** (**SI**). No impurity phases were detected, and all elements (Cu, Ag, In and Te) are distributed homogeneously on the micron scale. The actual chemical compositions of all samples determined by EDS measurements are presented in **Table 1**. Each value is close to the corresponding nominal composition. These results indicate that $CuInTe_2$ and $AgInTe_2$ can easily form a solid solution with any ratio. **Figure 2d** is a typical high resolution TEM image of $Cu_{0.8}Ag_{0.2}InTe_2$, and its corresponding selected area diffraction pattern is shown in **Figure 2e**. The diffraction pattern can be well indexed to the chalcopyrite structure along the [110] zone axis. The absence of Bragg spot splitting, extra spots, streaking or superlattice spots indicates the sample is a true solid solution, which further supports the XRD and elemental analyses above.

3.2 Electronic Transport Properties

Because of the relatively low carrier concentration (1.25×10^{18} cm^{-3} at 300 K, **Table 1**), the electrical conductivity of $CuInTe_2$ (20.5 S cm^{-1} at 300 K) is quite low in comparison with other conventional doped thermoelectric materials. As the temperature rises above 450 K, the electrical conductivity of $CuInTe_2$ linearly increases, then plateaus at $\approx$150 S cm^{-1} above 800 K, as shown in **Figure 3a**. With increasing Ag content, the electrical conductivity dramatically drops because of the extremely low carrier concentration (< 10^{14} cm^{-3}) of intrinsic $AgInTe_2$. However, the electrical conductivity of all samples exhibits similar temperature-dependent behavior: a linear increase with rising temperature and a drop at high temperature. This abnormal charge transport behavior has also been observed in other diamond-like compounds, such as $CuGaTe_2$[52] and $AgGaTe_2$[54], and was associated with a deep acceptor level.[65] The high temperature charge carrier concentration and mobility data of $Cu_{0.8}Ag_{0.2}InTe_2$, shown in **Figure 3b**, support the existence of the acceptor level. The charge carrier mobility in $Cu_{0.8}Ag_{0.2}InTe_2$ decreases with a $T^{-3/2}$ dependence in the temperature range of 400-813 K, which suggests that acoustic phonons dominate the charge carrier scattering at high temperature.[6, 66] Corresponding to the trend in electrical conductivity, the carrier concentration of $Cu_{0.8}Ag_{0.2}InTe_2$ significantly increases from 7.43×10^{17} cm^{-3} at 450 K to 2.02×10^{19} cm^{-3} at 773 K. The activation energy of the acceptor level can be determined by fitting the resistivity according to the Arrhenius equation: $\rho=\rho_0\times\exp(E_a/k_BT)$; here, ρ, E_a and k_B are the resistivity, activation energy and Boltzmann constant, respectively.[54] The obtained activation energy is 0.27 eV for the $Cu_{0.8}Ag_{0.2}InTe_2$ compound, a value much smaller than the optical band gap of the $Cu_{1-x}Ag_xInTe_2$ compounds (~0.93 eV), shown in **Figure 3c**. All these results are consistent with the existence of an important mid-gap acceptor level in the $Cu_{1-x}Ag_xInTe_2$ compounds.

To further clarify the electronic transport behavior of $Cu_{1-x}Ag_xInTe_2$, the low temperature carrier concentration and mobility for all samples are shown in **Figure S2** (**SI**). In contrast with the high temperature data, the low temperature carrier concentrations for all samples exhibit a weak temperature-dependent behavior, and the carrier mobility is governed by various scattering mechanisms at different temperatures. The electrical transport behavior of $Cu_{1-x}Ag_xInTe_2$ over a wide range of temperature can be divided into four distinct regimes, as displayed in **Figure 3d**. We take the $Cu_{0.8}Ag_{0.2}InTe_2$ compound as an example. (I) Initially, ionized impurities dominate the carrier scattering at low temperature (10-200 K), leading to the decline in resistivity with rising temperature. (II) As shown in **Figure 4a**, the acceptor level is empty below 450 K, and the sample just behaves as a degenerate semiconductor. Here alloy scattering dominates from 200 K to 450 K, resulting in a temperature-independent resistivity. (III) When the temperature exceeds 450 K, the acceptor level activates (**Figure 4b**), and the carrier concentration rises exponentially, yielding a linear temperature dependence in the resistivity. (IV) Above 750 K, all acceptor states have been occupied and the carrier concentration is almost constant; hence, the sample behaves as a degenerate semiconductor with the electrical resistivity increasing with rising temperature. Obviously, the acceptor level is crucial to the electronic transport properties and contributes to the relatively high electrical conductivity and power factor of $Cu_{1-x}Ag_xInTe_2$ at high temperature. Certainly, different types of intrinsic defects may exist in the $Cu_{1-x}Ag_xInTe_2$ compounds that could account for the temperature dependence of the carrier concentration. A full investigation of the defect status of this material is complex and will be the focus of future work.

The temperature-dependent Seebeck coefficient of $Cu_{1-x}Ag_xInTe_2$ follows the usual inverse relationship with respect to the temperature dependence of electrical conductivity, shown in **Figure 3e**. Besides, because of the decrease in carrier concentration, the Seebeck coefficient of $Cu_{1-x}Ag_xInTe_2$ increases with increasing Ag content, with Ag-rich compounds possessing values near 900 μVK^{-1} at room temperature, significantly larger than those of conventional thermoelectric materials.

The temperature dependence of the power factor is shown in **Figure 3f**. Due to the large drop in electrical conductivity, the power factor decreases with increasing Ag content, and the highest power factors for all samples were obtained at 750 K. Since this behavior is consistent with the carrier concentration, the power factor of the $Cu_{1-x}Ag_xInTe_2$ compounds would probably be enhanced by further increasing the carrier concentration.

In order to better understand the electronic transport properties of $Cu_{1-x}Ag_xInTe_2$ compounds, the electronic energy band structures and the corresponding projected density of states for $CuInTe_2$, $Cu_{0.5}Ag_{0.5}InTe_2$ and $AgInTe_2$ were calculated, as shown in **Figure 5**. Because of the same crystal structure and similar composition, the band structure of the different $Cu_{1-x}Ag_xInTe_2$ compounds are much alike, showing the multiply degenerate valence band maximum at the Γ point and a direct band gap. The valence band maximum of $Cu_{1-x}Ag_xInTe_2$ compounds is composed of a non-degenerate light-hole band and a doubly degenerate heavy-hole band. Since the energy difference between these bands is small, the valence bands at the Γ point are nearly triply degenerate, which leads to a decent p-type thermoelectric performance. Besides, for the $Cu_{1-x}Ag_xInTe_2$ compounds, the energy states near the valence band edge primarily come from the hybridization of 5p orbitals of Te, 3d orbitals of Cu and 4d orbitals of Ag. Besides, the density of states effective mass for $CuInTe_2$ is 0.21 m_0, which is somewhat lower than that of the $AgInTe_2$ compound (0.25 m_0), which together with the higher carrier density contribute to the better electronic transport properties in $CuInTe_2$.

3.3. Thermal Conductivity

The temperature dependence of the lattice thermal conductivity for all $Cu_{1-x}Ag_xInTe_2$ compounds is shown in **Figure 6a**. The room temperature lattice thermal conductivity of pristine $CuInTe_2$ is 5.65 $Wm^{-1}K^{-1}$. As the temperature increases, its thermal conductivity dramatically decreases reaching 0.92 $Wm^{-1}K^{-1}$ at 850 K because of the enhanced contribution of Umklapp processes.[6, 67] Moreover, with increasing Ag content, a large drop to 1.28 $Wm^{-1}K^{-1}$ at room temperature is observed in the lattice thermal conductivity of $Cu_{1-x}Ag_xInTe_2$, and an ultralow lattice thermal conductivity of 0.24 $Wm^{-1}K^{-1}$ was obtained for $Cu_{0.2}Ag_{0.8}InTe_2$ at 850 K.

Generally, the lattice thermal conductivity in a solid is closely relate to the sound velocity v, heat capacity C_v, and the phonon mean free path l via $\kappa_L = 1/3C_vvl$. **Figure 6b** depicts the measured room temperature sound velocities for $Cu_{1-x}Ag_xInTe_2$. Consistent with the lattice thermal conductivity, the sound velocity linearly decreases with increasing Ag content. The sound velocity generally describes how rapidly lattice vibrations propagate in a material and is chiefly determined by the strength of the chemical bonds, or equivalently, the anharmonicity of the crystal.[68] The decrease in sound velocity with Ag content indicates the $AgInTe_2$ compound is more inefficient transporting lattice vibrations than the $CuInTe_2$. Thus, the difference in chemical bond strength between Cu and Ag in the chalcopyrite structure should account for the difference in sound velocity, and this is crucial to the heat transport properties of the $Cu_{1-x}Ag_xInTe_2$ compounds.

In order to further understand the phonon transport behavior of $Cu_{1-x}Ag_xInTe_2$, (x=0, 0.5, 1) we performed DFT calculations of the phonon dispersions and corresponding projected phonon density of states, **Figure 7**. The phonon dispersion curves show intersections between acoustic phonons and low-frequency optical phonons for all compounds, as highlighted by the pink regions shown in **Figure 7**. This suggests there is strong coupling between acoustic phonons and low-frequency optical phonons in these materials. Obviously, the intersections decrease the Debye frequency (the highest frequency of the acoustic phonons) with increasing amount of Ag, suggesting higher lattice anharmonicity (**Figure S3 SI**) and enhanced phonon-phonon coupling in the Ag-rich compounds.

The projected phonon density of states clearly shows the change of the low-frequency phonon with Ag content. For the pristine $CuInTe_2$, most of the low-frequency phonons stem from the In and Te atoms, and the low-frequency peak is located around 50 cm^{-1}, as in **Figure 7b**. However, when substituting Cu with Ag in the structure, additional low-frequency phonons are introduced, and the low-frequency peak decreases to 40 cm^{-1} for $Cu_{0.5}Ag_{0.5}InTe_2$ and drops to around 30 cm^{-1} for $AgInTe_2$, see **Figure 7d and 7f**. The corresponding calculated average phonon velocities for $CuInTe_2$, $Cu_{0.5}Ag_{0.5}InTe_2$ and $AgInTe_2$ are 2451, 2334 and 2184 ms^{-1}, a trend consistent with our sound velocity measurements. These results suggest that the Ag atom introduces significant low-frequency optical phonons in the chalcopyrite structure, which couple to acoustic phonons inducing lower phonon velocities and higher lattice anharmonicity in the material.

The temperature dependence of the atomic displacement parameters (ADPs) for $CuInTe_2$ and $AgInTe_2$ were also obtained by first-principles molecular dynamics (MD) simulations, the results of which are shown in **Figure 8a**. For $CuInTe_2$, all atoms possess similar ADP values at the same temperature, indicating similar vibration amplitude behavior in the chalcopyrite structure. For $AgInTe_2$, the ADP values of In and Te are somewhat higher than the corresponding value for $CuInTe_2$. However, the Ag atom ADP is more than double the ADP of Cu. The larger ADP value of Ag suggests that it vibrates with greater amplitude around its equilibrium position than the In and Te. Physically, the large ADP values imply weak restoring forces on the vibrating atoms due to the existence of weak bonding and anharmonicity.

To further understand the bonding character of Cu and Ag in the chalcopyrite structure, we performed crystal orbital Hamiltonian populations (COHP) analysis on the electronic density of states. The COHP is the weighted density of states by the corresponding element of the Hamiltonian. By evaluating the COHP, we partition the band structure energy into bonding, nonbonding, and antibonding contributions. The positive values of COHP suggest bonding interactions that stabilize the structure, and negative COHP values imply anti-bonding interactions that destabilize the structure.[18] As shown in **Figure 8b**, the electron interactions of Cu-Te and Ag-Te are anti-bonding from -5 to -2.7 eV with greater negative values for the Ag case. The electrons turn to bonding interactions from -2.7 to -0.1 eV. Ag-Te bonding is evidently less favorable than the Cu-Te bonding in the chalcopyrite structure. Just as integrating the electronic DOS gives the number of electrons in the system, the integrated COHP hints towards the bond strength.[69] The larger the values of integrated COHP, the stronger bond strength is. As shown in **Figure 8c**, the integrated COHP of Ag has smaller values than Cu in a majority of energy range, suggesting weaker chemical bonding of Ag than Cu in the chalcopyrite structure. The theoretical calculations therefore suggest weaker Ag-Te chemical bonding in $AgInTe_2$ that results in the low-frequency vibrations causing the coupling between acoustic phonons and low-frequency optical phonons.

Heat capacities

In order to better understand the impact of the phonon coupling effect on the lattice thermal conductivity, we measured the low temperature heat capacities of the $Cu_{1-x}Ag_xInTe_2$ compounds. The plot of C_p/T^3 versus T in the temperature interval of 2-40 K is shown in **Figure 9a**. Obviously, a pronounced wide maximum around 10 K is observed in all samples, and the peak value increases with increasing Ag content. This peak structure is referred to as the Boson peak and is ascribed to an excess phonon density of states, which is associated with low-frequency optical modes and regarded as a sign of the coupling between low-frequency optical phonons and acoustic phonons.[70] The enhanced Boson peak with increasing Ag content suggests the enhancement of the phonon coupling effect in the material, which is consistent with the DFT calculation. The Boson peak behavior has already been observed in other intrinsic low thermal conductivity materials, such as $Cu_{17.6}Fe_{17.6}S_{32}$,[68] $CsSnBr_3$,[71] $AgGaTe_2$[54] and Cu_3SbSe_3[72], and can be discerned by the Debye-Einstein model[68, 73]:

$$C_p / T = \gamma + bT^2 + \sum_{i=1}^{n} A_i (\Theta_{Ei})^2 \cdot (T^2)^{-(3/2)} \cdot \frac{e^{\Theta_{Ei}/T}}{(e^{\Theta_{Ei}/T} - 1)^2} \tag{2}$$

Here, the first term represents the electronic contribution to the specific heat and is referred to as the Sommerfeld constant γ associated with the density-of-states effective mass and charge carrier concentration. The second term represents the Debye lattice contribution and is given as $b=C\cdot(12\pi^4 N_A k_B)/(5\Theta_D^3)$; here, N_A is Avogadro's number, k_B is the Boltzmann constant and Θ_D is the Debye temperature. The parameter C is defined as $C = 1 - \sum_i A_i / 3NR$, where N and R are the number of atoms per formula unit and the gas constant, respectively. The third term is the contribution of the localized Einstein oscillator modes that represent the low frequency phonon modes. Here, n is the number of Einstein modes, A_i is the amplitude of the i^{th} Einstein oscillator mode, and Θ_{Ei} is the corresponding Einstein temperature.

We can analyze the low temperature heat capacity data by the Debye-Einstein model, and the $Cu_{0.8}Ag_{0.2}InTe_2$ compound is selected as a canonical example here, as shown in **Figure 9b and 9c**. Obviously, the simple Debye model or the Debye +1 Einstein mode model fails to explain the experimental data. The low temperature heat capacity can sufficiently be described only by introducing two Einstein oscillators in the Debye host, which corroborates the existence of low-frequency phonons in the $Cu_{1-x}Ag_xInTe_2$ compounds. The fitting parameters obtained from the low temperature heat capacities of all samples are listed in **Table 2**. The pristine $CuInTe_2$ possesses a relatively low Debye temperature of 178 K, which decreases significantly with increasing Ag content, reaching a minimum of 135 K for $AgInTe_2$. The decrease in Debye temperature is ascribed to the depression of the Debye frequency by the added low-frequency optical phonons, leading to the enhanced phonon-phonon coupling effect with increasing Ag content. These results are consistent with the DFT calculations, as shown in **Figure 9d**.

Phonon resonance scattering

To assess the strength of phonon scattering and understand the impact of the phonon coupling effect on the lattice thermal conductivity, we employed the Debye-Callaway model to study the lattice thermal conductivity of $Cu_{0.8}Ag_{0.2}InTe_2$. The Debye-Callaway model is given by[68, 74]:

$$\kappa_L = \frac{k_B}{2\pi^2 v}\left(\frac{k_B}{\hbar}\right)^3 T^3 \int_0^{\Theta_D/T} \frac{x^4 e^x}{\tau_c^{-1}(e^x-1)^2}dx \tag{3}$$

Here k_B, v, Θ_D, and $\hbar$ are the Boltzmann constant, average sound velocity, Debye temperature, and the reduced Plank constant, respectively. x is expressed as $x = \hbar\omega / k_B T$, where ω is a given phonon frequency and τ_c represents the phonon relaxation time, which reflects the intensity of phonon scattering and generally contains a series of phonon scattering mechanisms. Here, we consider grain boundary scattering, τ_B, point defect scattering, τ_D, phonon-phonon Umklapp scattering, τ_U, and phonon resonance scattering, τ_R, as the important scattering mechanisms. Hence, the relaxation time can be expressed by Matthiessen's rule as[68, 73]:

$$\tau_c^{-1} = \tau_B^{-1} + \tau_D^{-1} + \tau_U^{-1} + \tau_R^{-1} = \frac{v}{L} + A\omega^4 + B\omega^2 T e^{-\Theta_D/3T} + \left[\frac{C_1\omega^2}{\left(\omega_1^2 - \omega^2\right)^2} + \frac{C_2\omega^2}{\left(\omega_2^2 - \omega^2\right)^2}\right] \tag{4}$$

where L stands for the grain size, constants A and B are the fitting parameters and the fourth term represents the phonon resonance scattering incorporated for the phonon scattering that is caused by the phonon coupling effect. Here C_1 and C_2 are proportional to the concentration of the oscillators and ω_1 and ω_2 are phonon resonance frequencies obtained from the low temperature heat capacity fitting results, i.e. the Einstein temperatures. Using the specified τ_c of **Eq. 3**, we fit the measured lattice thermal conductivity data of $Cu_{0.8}Ag_{0.2}InTe_2$ to **Eq. 2** and extracted the best-fit parameters, which are listed in **Table S1**.

With the resulting best-fit parameters, the phonon relaxation time τ versus phonon frequency ω for $Cu_{0.8}Ag_{0.2}InTe_2$ with different scattering mechanisms is plotted in **Figure 9e**. Here, the cutoff frequency is the Debye frequency, $\hbar\omega_D = k_B\theta_D$,[17] and all vibrational modes were considered. Obviously, except for the grain boundaries scattering, both point defect scattering, Umklapp scattering and phonon resonance scattering are effective to reduce the phonon relaxation time for $Cu_{0.8}Ag_{0.2}InTe_2$. Moreover, the phonon resonance scattering stemming from the Einstein oscillators introduce two localized minima around 5.5 and 8.6 THz. Thus, phonons with frequencies close to 5.5 and 8.6 THz are intensely scattered, leading to very short phonon relaxation times and very little contribution to the lattice thermal conductivity.

Figure 9f depicts the contribution of each scattering process to the lattice thermal conductivity of $Cu_{0.8}Ag_{0.2}InTe_2$. The U, B, P and R represent Umklapp scattering, grain boundary scattering, point defect scattering, and phonon resonance scattering, respectively.[68] We note that the phonon resonance scattering is able to reduce the lattice thermal conductivity by 57% at 850 K. The phonon mean free path and Grüneisen constants for all samples were calculated and are listed in **Table 3** (for details, see **SI** Section 5). The decrease in phonon mean free path and increase in the Grüneisen constant also supports the enhanced Umklapp scattering and phonon resonance scattering with greater Ag content Therefore, both the theoretical calculations and the experimental results suggest the coupling between low frequency optical phonons and heat carrying acoustic phonons is vital to the low thermal conductivity of $Cu_{1-x}Ag_xInTe_2$.

3.4. Optimization of electronic transport and *ZT* value through doping on the In sites

The temperature dependence of the figure of merit *ZT* for $Cu_{1-x}Ag_xInTe_2$ are depicted in **Figure 10**. By combining the low lattice thermal conductivity with a decent power factor, the highest *ZT* value of 1.07 is obtained at 850 K for $Cu_{0.8}Ag_{0.2}InTe_2$. Even though Ag is very effective in reducing the lattice thermal conductivity, it also degrades the electronic transport properties of $Cu_{1-x}Ag_xInTe_2$, thus limiting its *ZT* value. In order to further improve the thermoelectric performance of $Cu_{1-x}Ag_xInTe_2$, we targeted the In site for substitution doping with Cu^+ as a means to increase the hole carrier concentration and improve the electronic transport properties. We thus synthesized the $Cu_{0.8+y}Ag_{0.2}In_{1-y}Te_2$ (y=0~0.1) compositions.

The XRD patterns of all SPSed $Cu_{0.8+y}Ag_{0.2}In_{1-y}Te_2$ samples are shown in **Figure S4** (**SI**). all sample XRD patterns can be indexed to the chalcopyrite structure, except one tiny impurity peak around 27.6° was observed when $y \geq 0.05$. The XRD Bragg peak positions of the samples shift to higher diffraction angles with increasing Cu content because of the smaller atomic radius of Cu than that of In, suggesting the successful doping of Cu into In sites in the structure. Interestingly, however, the carrier concentration data obtained from Hall measurements suggest the Cu is not an effective dopant to enhance the hole density and the carrier concentration only increased slightly at high temperature region, as shown in **Figure S6 and Figure 12a**.

Unexpectedly, the carrier mobility is greatly improved by substituting Cu for In, especially in the low temperature region (**Figure 12b**). Remarkably, the carrier mobility increases sharply from 92 $cm^2V^{-1}s^{-1}$ to 212 $cm^2V^{-1}s^{-1}$ at room temperature, a near 100% increase. As the temperature increases the mobility slowly decreases until about 600 K when it drops rapidly to about 50 $cm^2V^{-1}s^{-1}$ becoming equal to that of the undoped sample, see Figure 12b Generally, dopants become scattering centers in the lattice, decreasing the carrier mobility. Evidently, in this case, Cu substitution is able to reduce carrier scattering, enhancing the carrier mobility. **Figure 12c** depicts the phonon mean free path (PMFP) and the carrier mean free path (CMFP) for $Cu_{0.8}Ag_{0.2}InTe_2$, $Cu_{0.85}Ag_{0.2}In_{0.95}Te_2$ and $Cu_{0.89}Ag_{0.2}In_{0.91}Te_2$. Obviously, the CMFP of the Cu substitution compounds are enhanced in the range 300-600 K, then decrease with increasing temperature, finally, the CMFP for all samples becomes the same above 600 K. Importantly, the order of magnitudes for PMFP and CMFP is very closed in the pristine $Cu_{0.8}Ag_{0.2}InTe_2$ compound, which is $2{\sim}3\times10^{-9}$ m at 300 K. In most of the thermoelectric materials, the CMFP is usually much larger than the PMFP, (take zone melted $Bi_{0.5}Sb_{1.5}Te_3$ alloy as an example, its CMFP is 26 nm and PMFP is 1.2 nm)[27]. However, in our case, the CMFP is close to the PMFP in $Cu_{0.8}Ag_{0.2}InTe_2$, implying the electron phonon scattering should be strong in the lattice at low temperature. Besides, this carrier scattering can be greatly reduced by substituting Cu for In, which in turn, increases the carrier mobility with Cu doping. This substantial increase in hole mobility upon doping on the In site is both surprising and intriguing. It implies that hole scattering has been significantly reduced as the In^{3+} ions have been replaced by Cu^+ or Ag^+ ions. One way we can intuitively understand this effect is that triply charged cations such In^{3+} are expected to scatter carriers much more strongly than singly charged ones. If this kind of scattering is diminished, then the mean free path of the carriers would be increased as shown in **Figure 12c**. Besides, since the carrier density dramatically increases with increasing temperature, which in turn enhances the electron-electron scattering and leads to the decline of mobility above 600 K.

The increase in carrier concentration and carrier mobility lead to the enhanced electrical conductivity and the improvement in power factor, **Figure 11a and 11c**. Importantly, since the lattice thermal conductivity of $Cu_{1-x}Ag_xInTe_2$ is governed by the phonon coupling effect, which derived from Ag, the low thermal conductivity of $Cu_{1-x}Ag_xInTe_2$ is also preserved in the Cu-doped samples. Overall, the *ZT* value is improved because of the enhanced power factor. A comparison of the thermoelectric properties clearly illustrating the optimization path across the $CuInTe_2$, $Cu_{0.8}Ag_{0.2}InTe_2$ and Cu-doped $Cu_{0.8}Ag_{0.2}InTe_2$ samples is shown in **Figure 13**. Evidently, Ag alloying is very effective to suppress the heat transport in $CuInTe_2$, and an extremely low lattice thermal conductivity of 0.47 $Wm^{-1}K^{-1}$ was obtained for $Cu_{0.8}Ag_{0.2}InTe_2$ at 850 K. Although Ag also degrades the electronic transport properties of the samples, we found the Cu doping is able to improve the electrical conductivity and preserve the low thermal conductivity of the compound. A respectable power factor of 8.82 $\mu Wcm^{-1}K^{-2}$ was achieved for the 9% Cu-doped $Cu_{0.8}Ag_{0.2}InTe_2$ sample. Finally, a maximum *ZT* value of 1.58 was obtained for the $Cu_{0.89}Ag_{0.2}In_{0.91}Te_2$ compound at 850 K, which represents an 84% enhancement over the value for the pristine $CuInTe_2$. This *ZT* value is larger than all reported element-doped $CuInTe_2$ materials to date.

4. Conclusion

This work clarifies the significant role of phonon coupling in the low thermal conductivity of $Cu_{1-x}Ag_xInTe_2$, and demonstrates a great improvement in thermoelectric performance by Ag alloying and composition control. The electronic transport properties suggest an important intrinsic acceptor level is present in $Cu_{1-x}Ag_xInTe_2$ that gives rise to the temperature-dependent carrier concentration and leads to superior power factor at high temperature. Ag alloying is very effective in suppressing heat conduction in $Cu_{1-x}Ag_xInTe_2$, leading to an ultralow lattice thermal conductivity of 0.24 $Wm^{-1}K^{-1}$ for $Cu_{0.2}Ag_{0.8}InTe_2$ at 850 K. The electronic structure calculations suggest relatively weak chemical bonding of Ag-Te leading to larger ADPs, as well as the low-frequency optical phonons. The Ag-induced low frequency phonons are strongly coupled with the heat carrying acoustic phonons, decreasing the Debye temperature and the phonon velocity. The resultant scattering by the low-frequency oscillators greatly diminish the phonon relaxation times. Thus, all factors lead to a low lattice thermal conductivity in $Cu_{1-x}Ag_xInTe_2$. Furthermore, Cu doping is able to improve the power factor of $Cu_{0.8}Ag_{0.2}InTe_2$ by increasing the charge carrier mobility, while simultaneously preserving the low thermal conductivity. As a result, a maximum *ZT* of ~ 1.6 is achieved at 850 K for the $Cu_{0.89}Ag_{0.2}In_{0.91}Te_2$ compound. The key finding in this work that the combination of Ag alloying on the Cu sites, and Cu doping on the In^{3+} sites, accomplishes two independent tasks: one being the strong reduction of the thermal conductivity and the other, surprisingly, the increase in hole carrier mobility. This is a rare combination of effects and, in fact, we believe unique among thermoelectric materials systems. As such, our work offers a referential strategy to further optimize the thermoelectric performance of other diamond-like materials.

Author contributions

H.X. performed the sample synthesis, structural characterization, optical measurements, and thermoelectric transport property measurements. S.C. and V.P.D. performed the TEM analyses. T.P.B. and C.U. performed the Hall measurement. S.H. and C.W. carried out the density functional theory calculations. All of the authors analyzed the data and discussed the underlying physics. H.X. and M.G.K. wrote the paper with contributions from the other authors. The manuscript reflects the contributions of all authors.

Competing interests

The authors declare no competing interests.

Acknowledgements

This work was primarily supported by a grant from the U.S. Department of Energy, Office of Science, and Office of Basic Energy Sciences under Award Number DE-SC0014520; This work also made use of the EPIC facility of Northwestern University's NU*ANCE* Center, which has received support from the Soft and Hybrid Nanotechnology Experimental (*SHyNE*) Resource (NSF ECCS-1542205); the MRSEC program (NSF DMR-1720139) at the Materials Research Center; the International Institute for Nanotechnology (IIN); the Keck Foundation; and the State of Illinois, through the IIN. User Facilities are supported by the Office of Science of the U.S. Department of Energy under Contract No. DE-AC02-06CH11357 and DE-AC02-05CH11231.

Supporting Information

SEM; XRD; lattice thermal conductivity calculation; phonon calculations; Gruneisen parameters; optical absorption spectra

Reference

1. T. M. Tritt and M. A. Subramanian, *MRS Bulletin*, 2011, **31**, 188-198.
2. G. J. Snyder and E. S. Toberer, *Nat Mater*, 2008, **7**, 105-114.
3. L. E. Bell, *Science*, 2008, **321**, 1457-1461.
4. T. Zhu, Y. Liu, C. Fu, J. P. Heremans, J. G. Snyder and X. Zhao, *Adv Mater*, 2017, **29**, 1605884.
5. J. He and T. M. Tritt, *Science*, 2017, **357**, 6358.
6. H. J. Goldsmid, Introduction to Thermoelectricity. Springer Berlin Heidelberg: Heidelberg, 2016.
7. X. Su, P. Wei, H. Li, W. Liu, Y. Yan, P. Li, C. Su, C. Xie, W. Zhao, P. Zhai, Q. Zhang, X. Tang and C. Uher, *Adv Mater*, 2017, **29**, 1602013.
8. Y. Pei, X. Shi, A. LaLonde, H. Wang, L. Chen and G. J. Snyder, *Nature*, 2011, **473**, 66-69.
9. W. Liu, X. Tan, K. Yin, H. Liu, X. Tang, J. Shi, Q. Zhang and C. Uher, *Phys. Rev. Lett.*, 2012, **108**, 166601.
10. L.-D. Zhao, G. Tan, S. Hao, J. He, Y. Pei, H. Chi, H. Wang, S. Gong, H. Xu, V. P. Dravid, C. Uher, G. J. Snyder, C. Wolverton and M. G. Kanatzidis, *Science*, 2016, **351**, 141-144.
11. A. J. Minnich, M. S. Dresselhaus, Z. F. Ren and G. Chen, *Energy Environ. Sci.*, 2009, **2**, 466.
12. J. P. Heremans, C. M. Thrush and D. T. Morelli, *Phys. Rev. B*, 2004, **70**, 115334.
13. K. Biswas, J. He, I. D. Blum, C. I. Wu, T. P. Hogan, D. N. Seidman, V. P. Dravid and M. G. Kanatzidis,

Nature, 2012, **489**, 414-418.

14. B. Poudel, Q. Hao, Y. Ma, Y. Lan, A. Minnich, B. Yu, X. Yan, D. Wang, A. Muto, D. Vashaee, X. Chen, J. Liu, M. S. Dresselhaus, G. Chen and Z. Ren, *Science*, 2008, **320**, 634-638.
15. J.-F. Li, W.-S. Liu, L.-D. Zhao and M. Zhou, *NPG Asia Mater*, 2010, **2**, 152-158.
16. J. He, M. G. Kanatzidis and V. P. Dravid, *Mater. Today*, 2013, **16**, 166-176.
17. H. Xie, X. Su, S. Hao, C. Zhang, Z. Zhang, W. Liu, Y. Yan, C. Wolverton, X. Tang and M. G. Kanatzidis, *J. Am. Chem. Soc.*, 2019, **141**, 18900-18909.
18. Z.-Z. Luo, S. Hao, X. Zhang, X. Hua, S. Cai, G. Tan, T. P. Bailey, R. Ma, C. Uher, C. Wolverton, V. P. Dravid, Q. Yan and M. G. Kanatzidis, *Energy Environ. Sci.*, 2018, **11**, 3220-3230.
19. J. M. Hodges, S. Hao, J. A. Grovogui, X. Zhang, T. P. Bailey, X. Li, Z. Gan, Y. Y. Hu, C. Uher, V. P. Dravid, C. Wolverton and M. G. Kanatzidis, *J. Am. Chem. Soc.*, 2018, **140**, 18115-18123.
20. A. Banik, T. Ghosh, R. Arora, M. Dutta, J. Pandey, S. Acharya, A. Soni, U. V. Waghmare and K. Biswas, *Energy Environ. Sci.*, 2019, **12**, 589-595.
21. S. Cai, S. Hao, Z.-Z. Luo, X. Li, I. Hadar, T. P. Bailey, X. Hu, C. Uher, Y.-Y. Hu, C. Wolverton, V. P. Dravid and M. G. Kanatzidis, *Energy Environ. Sci.*, 2020, **13**, 200-211.
22. L. D. Zhao, S. H. Lo, Y. Zhang, H. Sun, G. Tan, C. Uher, C. Wolverton, V. P. Dravid and M. G. Kanatzidis, *Nature*, 2014, **508**, 373-377.
23. W. He, D. Wang, H. Wu, Y. Xiao, Y. Zhang, D. He, Y. Feng, Y.-J. Hao, J.-F. Dong, R. Chetty, L. Hao, D. Chen, J. Qin, Q. Yang, X. Li, J.-M. Song, Y. Zhu, W. Xu, C. Niu, X. Li, G. Wang, C. Liu, M. Ohta, S. J. Pennycook, J. He, J.-F. Li and L.-D. Zhao, *Science*, 2019, **365**, 1418-1424.
24. J. Mao, H. Zhu, Z. Ding, Z. Liu, G. A. Gamage, G. Chen and Z. Ren, *Science*, 2019, **365**, 495-498.
25. C. Fu, S. Bai, Y. Liu, Y. Tang, L. Chen, X. Zhao and T. Zhu, *Nat. Commun.*, 2015, **6**, 8144.
26. G. Tan, F. Shi, S. Hao, H. Chi, L. D. Zhao, C. Uher, C. Wolverton, V. P. Dravid and M. G. Kanatzidis, *J. Am. Chem. Soc.*, 2015, **137**, 5100-5112.
27. Y. Zheng, Q. Zhang, X. Su, H. Xie, S. Shu, T. Chen, G. Tan, Y. Yan, X. Tang, C. Uher and G. J. Snyder, *Adv. Energy Mater.*, 2015, **5**, 1401391.
28. G. Zheng, X. Su, H. Xie, Y. Shu, T. Liang, X. She, W. Liu, Y. Yan, Q. Zhang, C. Uher, M. G. Kanatzidis and X. Tang, *Energy Environ. Sci.*, 2017, **10**, 2638-2652.
29. R. Deng, X. Su, S. Hao, Z. Zheng, M. Zhang, H. Xie, W. Liu, Y. Yan, C. Wolverton, C. Uher, M. G. Kanatzidis and X. Tang, *Energy Environ. Sci.*, 2018, **11**, 1520-1535.
30. L.-P. Hu, T.-J. Zhu, Y.-G. Wang, H.-H. Xie, Z.-J. Xu and X.-B. Zhao, *NPG Asia Mater*, 2014, **6**, e88.
31. Y. Pan and J.-F. Li, *NPG Asia Mater*, 2016, **8**, e275.
32. Y. Pei, H. Wang, Z. M. Gibbs, A. D. LaLonde and G. J. Snyder, *NPG Asia Mater*, 2012, **4**, e28.
33. Y. Pei, J. Lensch-Falk, E. S. Toberer, D. L. Medlin and G. J. Snyder, *Adv. Funct. Mater.*, 2011, **21**, 241-249.
34. K. Biswas, J. He, Q. Zhang, G. Wang, C. Uher, V. P. Dravid and M. G. Kanatzidis, *Nat. Chem.*, 2011, **3**, 160-166.
35. Q. Zhang, Q. Song, X. Wang, J. Sun, Q. Zhu, K. Dahal, X. Lin, F. Cao, J. Zhou, S. Chen, G. Chen, J. Mao and Z. Ren, *Energy Environ. Sci.*, 2018, **11**, 933-940.
36. P.-a. Zong, R. Hanus, M. Dylla, Y. Tang, J. Liao, Q. Zhang, G. J. Snyder and L. Chen, *Energy Environ. Sci.*, 2017, , **10**, 183-191.
37. X. Meng, Z. Liu, B. Cui, D. Qin, H. Geng, W. Cai, L. Fu, J. He, Z. Ren and J. Sui, *Adv. Energy Mater.*, 2017, **7**, 1602582.
38. Y. Tang, R. Hanus, S. W. Chen and G. J. Snyder, *Nat. Commun.*, 2015, **6**, 7584.

39. W. Zhao, Z. Liu, Z. Sun, Q. Zhang, P. Wei, X. Mu, H. Zhou, C. Li, S. Ma, D. He, P. Ji, W. Zhu, X. Nie, X. Su, X. Tang, B. Shen, X. Dong, J. Yang, Y. Liu and J. Shi, *Nature*, 2017, **549**, 247-251.
40. Z. Zheng, X. Su, R. Deng, C. C. Stoumpos, H. Xie, W. Liu, Y. Yan, S. Hao, C. Uher, C. Wolverton, M. G. Kanatzidis and X. Tang, *J. Am. Chem. Soc.*, 2018, **140**, 2673-2686..
41. J. Li, X. Zhang, Z. Chen, S. Lin, W. Li, J. Shen, I. T. Witting, A. Faghaninia, Y. Chen, A. Jain, L. Chen, G. J. Snyder and Y. Pei, *Joule*, 2018, **2**, 976-987.
42. M. Hong, Y. Wang, W. Liu, S. Matsumura, H. Wang, J. Zou and Z.-G. Chen, *Adv. Energy Mater.*, 2018, **8**, 1801837.
43. M. Hong, Z. G. Chen, L. Yang, Y. C. Zou, M. S. Dargusch, H. Wang and J. Zou, *Adv Mater*, 2018, **30**, 1705942.
44. L. Wu, X. Li, S. Wang, T. Zhang, J. Yang, W. Zhang, L. Chen and J. Yang, *NPG Asia Mater*, 2017, **9**, e343.
45. R. Liu, L. Xi, H. Liu, X. Shi, W. Zhang and L. Chen, *Chem. Commun*, 2012, **48**, 3818-3820.
46. Y. Luo, J. Yang, Q. Jiang, W. Li, D. Zhang, Z. Zhou, Y. Cheng, Y. Ren and X. He, *Adv. Energy Mater.*, 2016, **6**, 1600007.
47. R. Liu, Y. Qin, N. Cheng, J. Zhang, X. Shi, Y. Grin and L. Chen, *Inorg. Chem. Front.*, 2016, **3**, 1167-1177.
48. J. Yang, S. Chen, Z. Du, X. Liu and J. Cui, *Dalton Trans.*, 2014, **43**, 15228-15236.
49. W. D. Carr and D. T. Morelli, *J. Alloys Compd.*, 2015, **630**, 277-281.
50. J. Shen, X. Zhang, Z. Chen, S. Lin, J. Li, W. Li, S. Li, Y. Chen and Y. Pei, *J. Mater. Chem. A*, 2017, **5**, 5314-5320.
51. J. Cui, Y. Li, Z. Du, Q. Meng and H. Zhou, *J. Mater. Chem. A*, 2013, **1**, 677-683.
52. T. Plirdpring, K. Kurosaki, A. Kosuga, T. Day, S. Firdosy, V. Ravi, G. J. Snyder, A. Harnwunggmoung, T. Sugahara, Y. Ohishi, H. Muta and S. Yamanaka, *Adv Mater*, 2012, **24**, 3622-3626.
53. A. Yusufu, K. Kurosaki, A. Kosuga, T. Sugahara, Y. Ohishi, H. Muta and S. Yamanaka, *Appl. Phys. Lett.*, 2011, **99**, 061902.
54. X. Su, N. Zhao, S. Hao, C. C. Stoumpos, M. Liu, H. Chen, H. Xie, Q. Zhang, C. Wolverton, X. Tang and M. G. Kanatzidis, *Adv. Funct. Mater.*, 2018, **29**, 1806534.
55. J. Zhang, R. Liu, N. Cheng, Y. Zhang, J. Yang, C. Uher, X. Shi, L. Chen and W. Zhang, *Adv Mater*, 2014, **26**, 3848-3853.
56. A. M. Moustafa, E. A. El-Sayad and G. B. Sakr, *Cryst. Res. Technol.*, 2004, **39**, 266-273.
57. P. Prabukanthan and R. Dhanasekaran, *Mater. Res. Bull.*, 2008, **43**, 1996-2004.
58. Y. Luo, J. Yang, Q. Jiang, W. Li, Y. Xiao, L. Fu, D. Zhang, Z. Zhou and Y. Cheng, *Nano Energy*, 2015, **18**, 37-46.
59. D. T. Morelli, V. Jovovic and J. P. Heremans, *Phys. Rev. Lett.*, 2008, **101**, 035901.
60. J. P. Perdew, J. A. Chevary, S. H. Vosko, K. A. Jackson, M. R. Pederson, D. J. Singh and C. Fiolhais, *Phys. Rev. B*, 1992, **46**, 6671-6687.
61. G. Kresse and J. Furthmüller, *Phys. Rev. B*, 1996, **54**, 11169-11186.
62. J. P. Perdew, K. Burke and M. Ernzerhof, *Phys. Rev. Lett.*, 1996, **77**, 3865-3868.
63. A. Togo and I. Tanaka, *Scr. Mater.*, 2015, **108**, 1-5.
64. K. Parlinski, Z. Q. Li and Y. Kawazoe, *Phys. Rev. Lett.*, 1997, **78**, 4063-4066.
65. J. Zhang, L. Huang, C. Zhu, C. Zhou, B. Jabar, J. Li, X. Zhu, L. Wang, C. Song, H. Xin, D. Li and X. Qin, *Adv Mater*, 2019, **31**, e1905210.
66. H. Xie, X. Su, G. Zheng, T. Zhu, K. Yin, Y. Yan, C. Uher, M. G. Kanatzidis and X. Tang, *Adv. Energy*

Mater., 2016, **7**, 1601299.

67. H. Xie, X. Su, Y. Yan, W. Liu, L. Chen, J. Fu, J. Yang, C. Uher and X. Tang, *NPG Asia Mater*, 2017, **9**, e390.
68. H. Xie, X. Su, X. Zhang, S. Hao, T. P. Bailey, C. C. Stoumpos, A. P. Douvalis, X. Hu, C. Wolverton, V. P. Dravid, C. Uher, X. Tang and M. G. Kanatzidis, *J. Am. Chem. Soc.*, 2019, **141**, 10905-10914.
69. S. Boudin, C. Felser and F. Studer, *Solid State Sci.*, 2003, **5**, 741-744.
70. M. K. Jana, K. Pal, A. Warankar, P. Mandal, U. V. Waghmare and K. Biswas, *J. Am. Chem. Soc.*, 2017, **139**, 4350-4353.
71. H. Xie, S. Hao, J. Bao, T. J. Slade, G. J. Snyder, C. Wolverton and M. G. Kanatzidis, *J. Am. Chem. Soc.*, 2020, **142**, 9553-9563.
72. W. Qiu, L. Xi, P. Wei, X. Ke, J. Yang and W. Zhang, *Proc. Natl. Acad. Sci. U. S. A.*, 2014, **111**, 15031-15035.
73. H. Liu, J. Yang, X. Shi, S. A. Danilkin, D. Yu, C. Wang, W. Zhang and L. Chen, *J Materiomics*, 2016, **2**, 187-195.
74. P. Ying, X. Li, Y. Wang, J. Yang, C. Fu, W. Zhang, X. Zhao and T. Zhu, *Adv. Funct. Mater.*, 2017, **27**, 1604145.

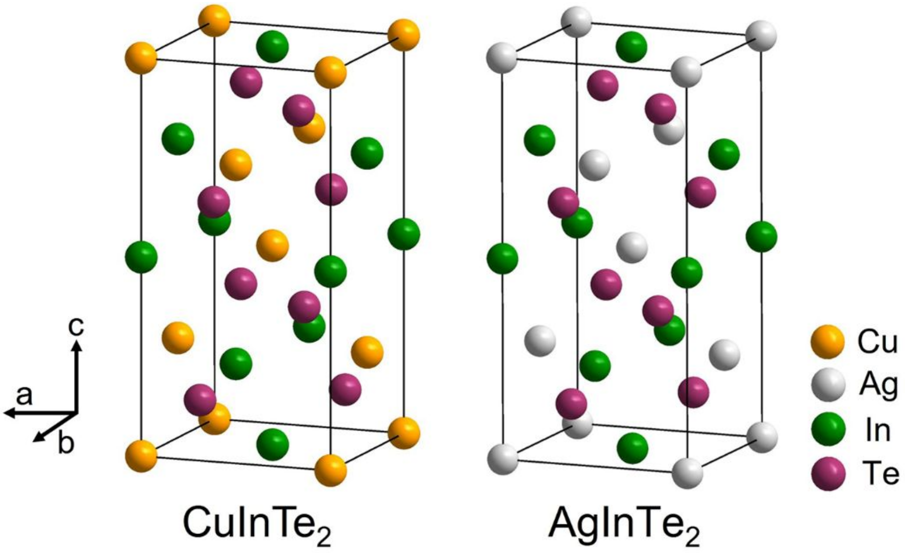

Figure 1. Crystal structure of CuInTe$_2$ and AgInTe$_2$.

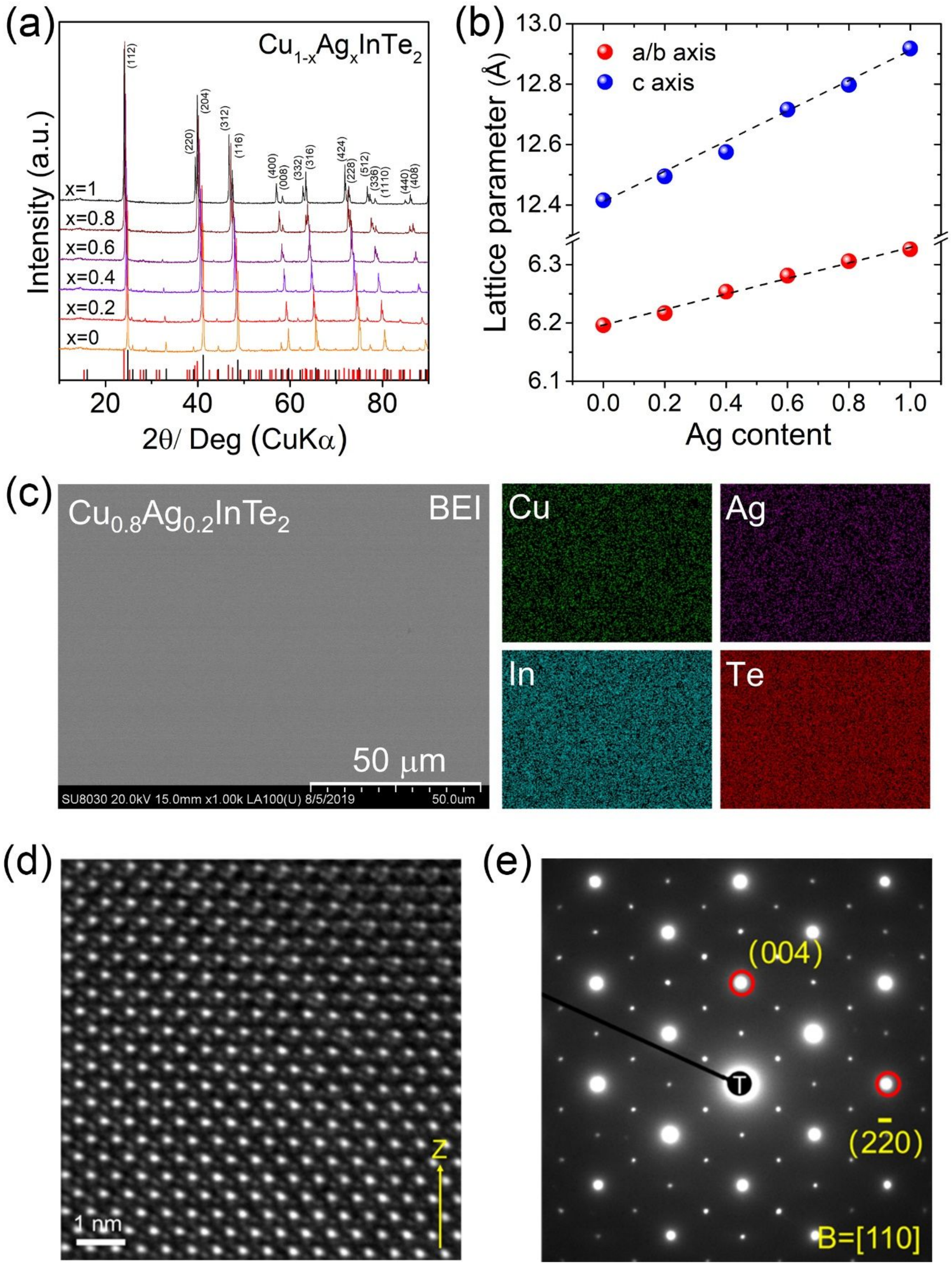

Figure 2. (a) XRD patterns of SPS-sintered $Cu_{1-x}Ag_xInTe_2$ (x = 0, 0.2, 0.4, 0.6, 0.8 and 1), the indices of crystal planes for $AgInTe_2$ as shown in figure; (b) lattice parameters of $Cu_{1-x}Ag_xInTe_2$; (c) BSE images of the polished surfaces and element maps by EDS for $Cu_{0.8}Ag_{0.2}InTe_2$; (d) high-resolution TEM image of $Cu_{0.8}Ag_{0.2}InTe_2$ taken along [110] zone axis. (e) corresponding selected area diffraction pattern along [110] zone axis. We observed no

evidence for secondary phases being present in the sample.

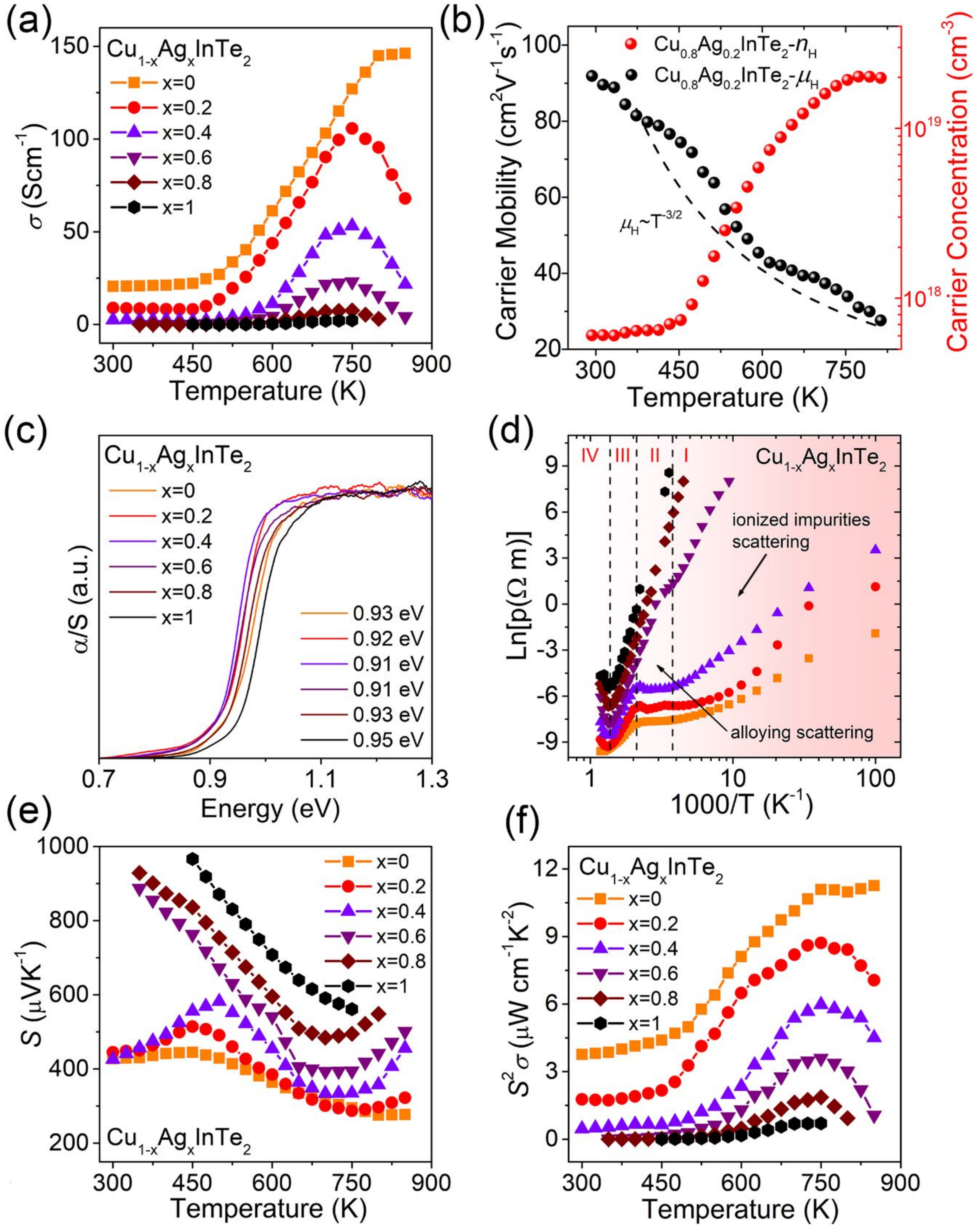

Figure 3. (a) The temperature dependence of electrical conductivity for $Cu_{1-x}Ag_xInTe_2$ compounds; (b) high temperature charge carrier concentration and mobility for the $Cu_{0.8}Ag_{0.2}InTe_2$ compound; (c) optical absorption spectra of $Cu_{1-x}Ag_xInTe_2$ compounds; (d) the temperature dependence of resistivity, plotted as ln(*p*) versus 1000/T; The temperature dependence of (e) Seebeck coefficient, and (f) power factor of $Cu_{1-x}Ag_xInTe_2$ compounds;

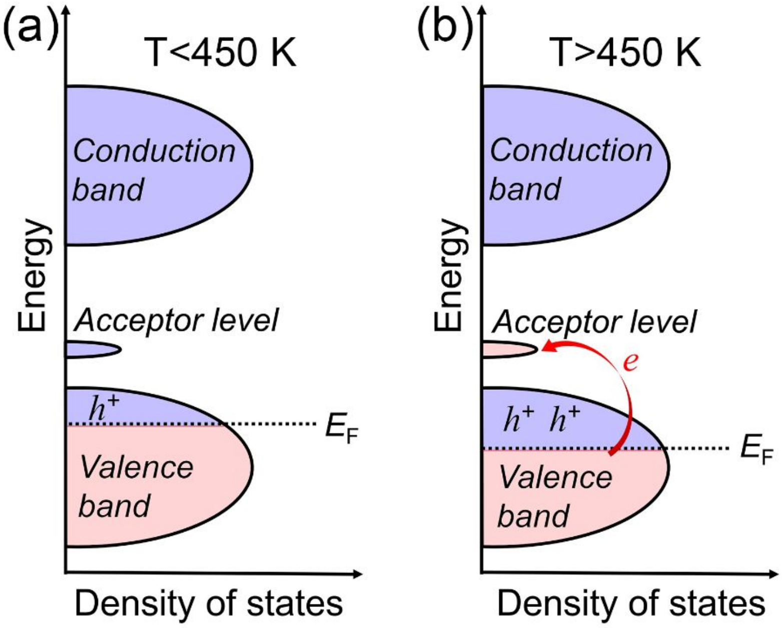

Figure 4. Schematic diagrams of the role of the acceptor level in electronic transport. (a) At low temperature, the acceptor level is empty, and the sample behaves as a degenerate semiconductor. (b) Because of the small energy gap between the acceptor level and the valence band, with rising temperature, part of electrons is excited and trapped by the acceptor level, which in turn increases the hole density in the material.

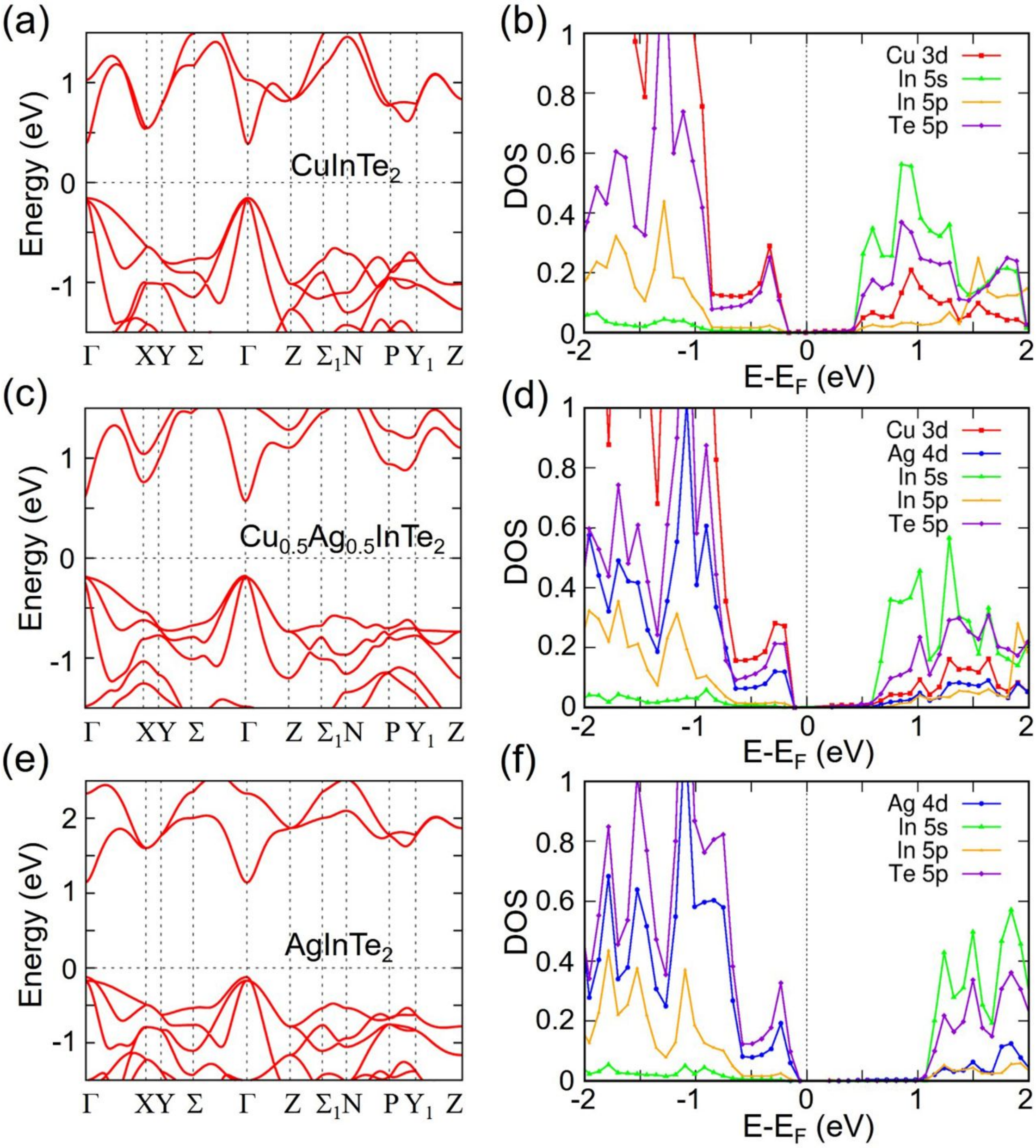

Figure 5. The electronic energy band structures for (a) $CuInTe_2$, (c) $Cu_{0.5}Ag_{0.5}InTe_2$ and (e) $AgInTe_2$. The electronic density of states for (b) $CuInTe_2$, (d) $Cu_{0.5}Ag_{0.5}InTe_2$ and (f) $AgInTe_2$.

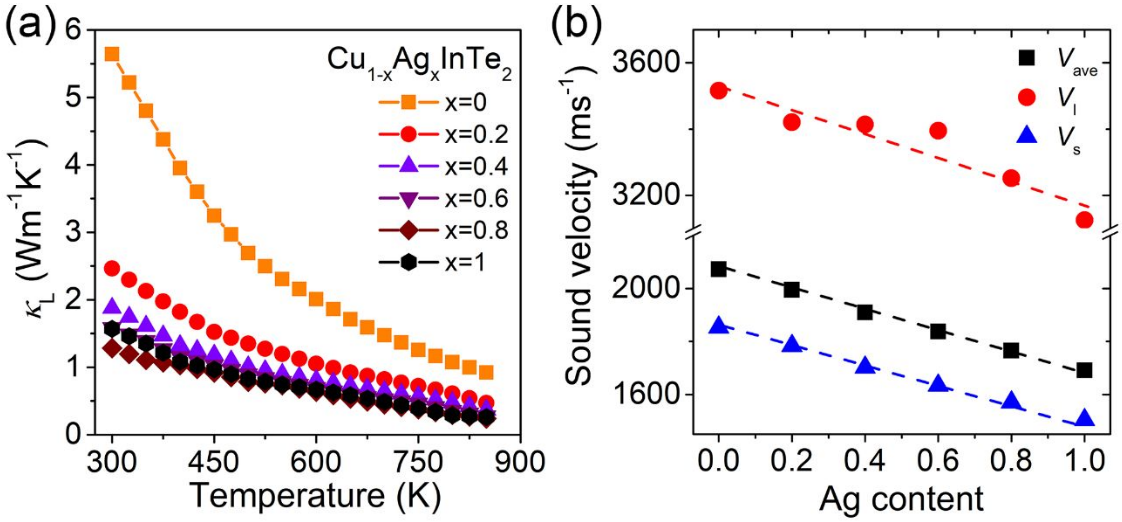

Figure 6. (a) The lattice thermal conductivity and (b) the sound velocity for $Cu_{1-x}Ag_xInTe_2$ (x = 0, 0.2, 0.4, 0.6, 0.8 and 1).

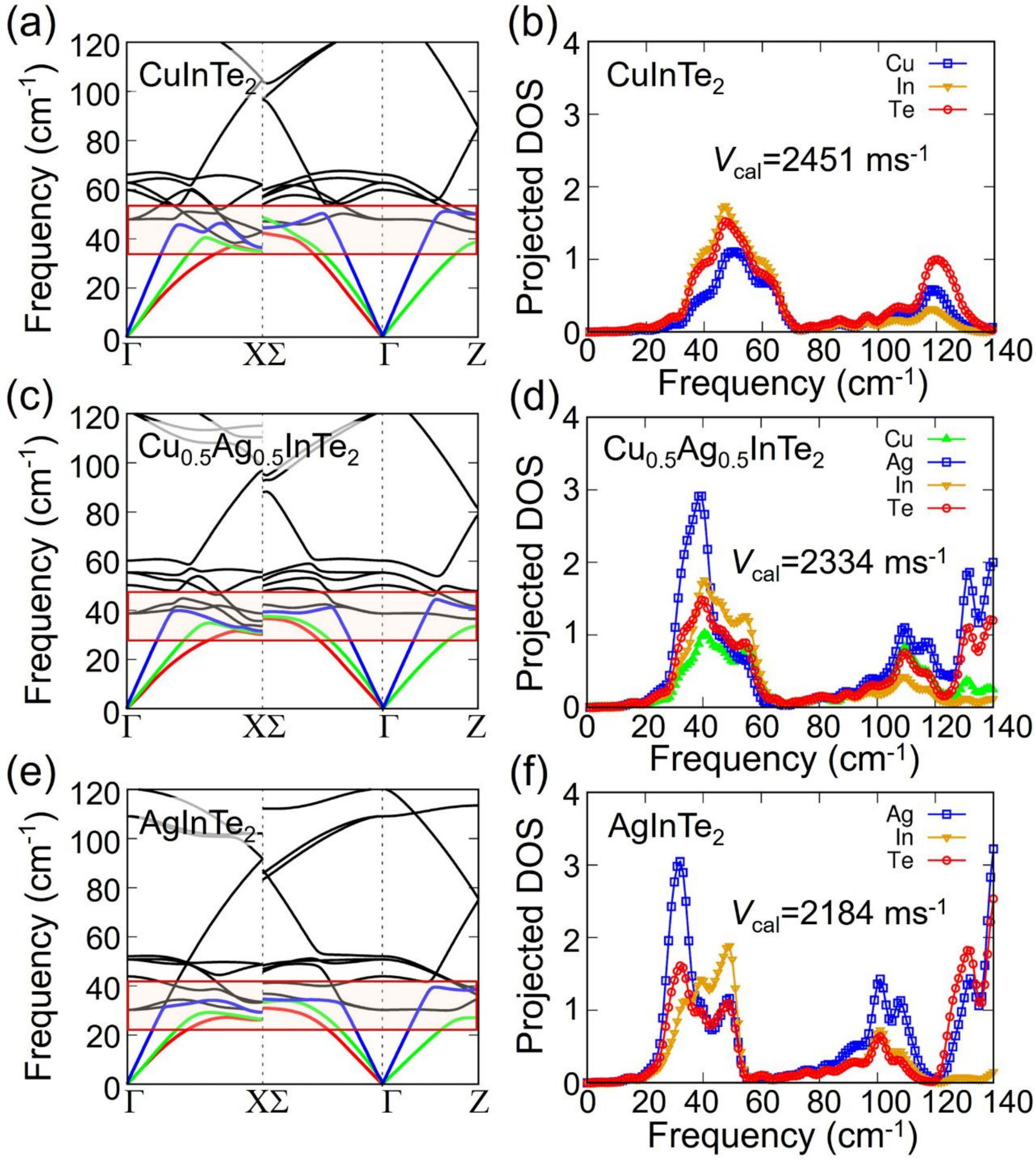

Figure 7. DFT calculated phonon dispersions and corresponding projected phonon density of states, respectively, for (a, b) $CuInTe_2$, (c, d) $Cu_{0.5}Ag_{0.5}InTe_2$, and (e, f) $AgInTe_2$.

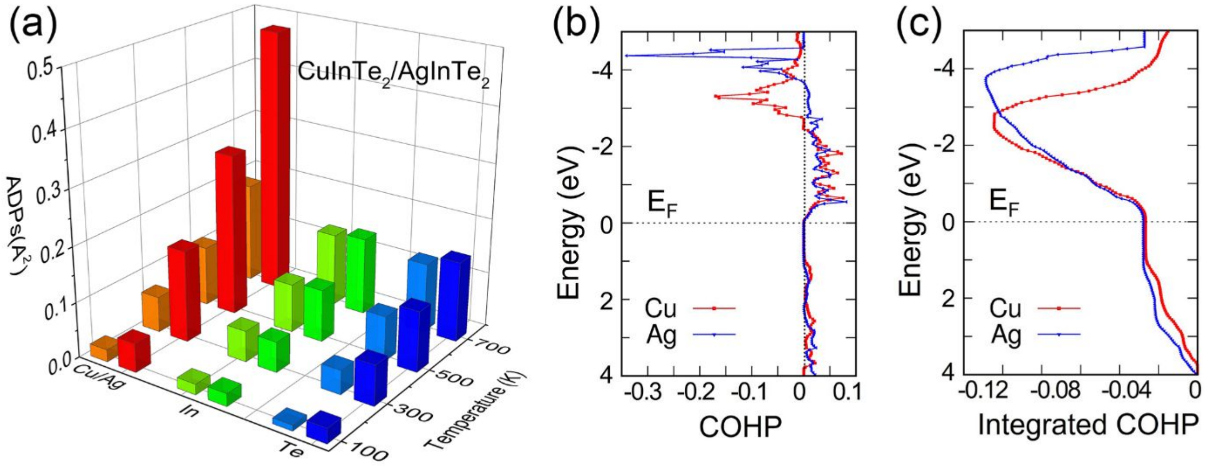

Figure 8. (a) Calculated atomic displacement parameters (ADPs) of $CuInTe_2$ and $AgInTe_2$; (b) The crystal orbital Hamiltonian populations (COHP) of Cu and Ag. The so-called COHP is the weighted density of states by the corresponding element of the Hamiltonian. By evaluating the COHP, we partition the band structure energy into bonding (positive values), nonbonding, and antibonding (negative values) contributions. The positive values of COHP suggest bonding interactions that stabilize the structure, and negative COHP values imply anti-bonding interactions that destabilize the structure. (c) The integrated COHP of Cu and Ag. By integrating the COHP, a measure of the bond strength can be obtained. The larger the value of integrated COHP, the stronger bond strength. Here the integrated COHP of Ag has smaller values than Cu in a majority of energy range, suggesting weaker chemical bonding of Ag than Cu in the chalcopyrite structure.

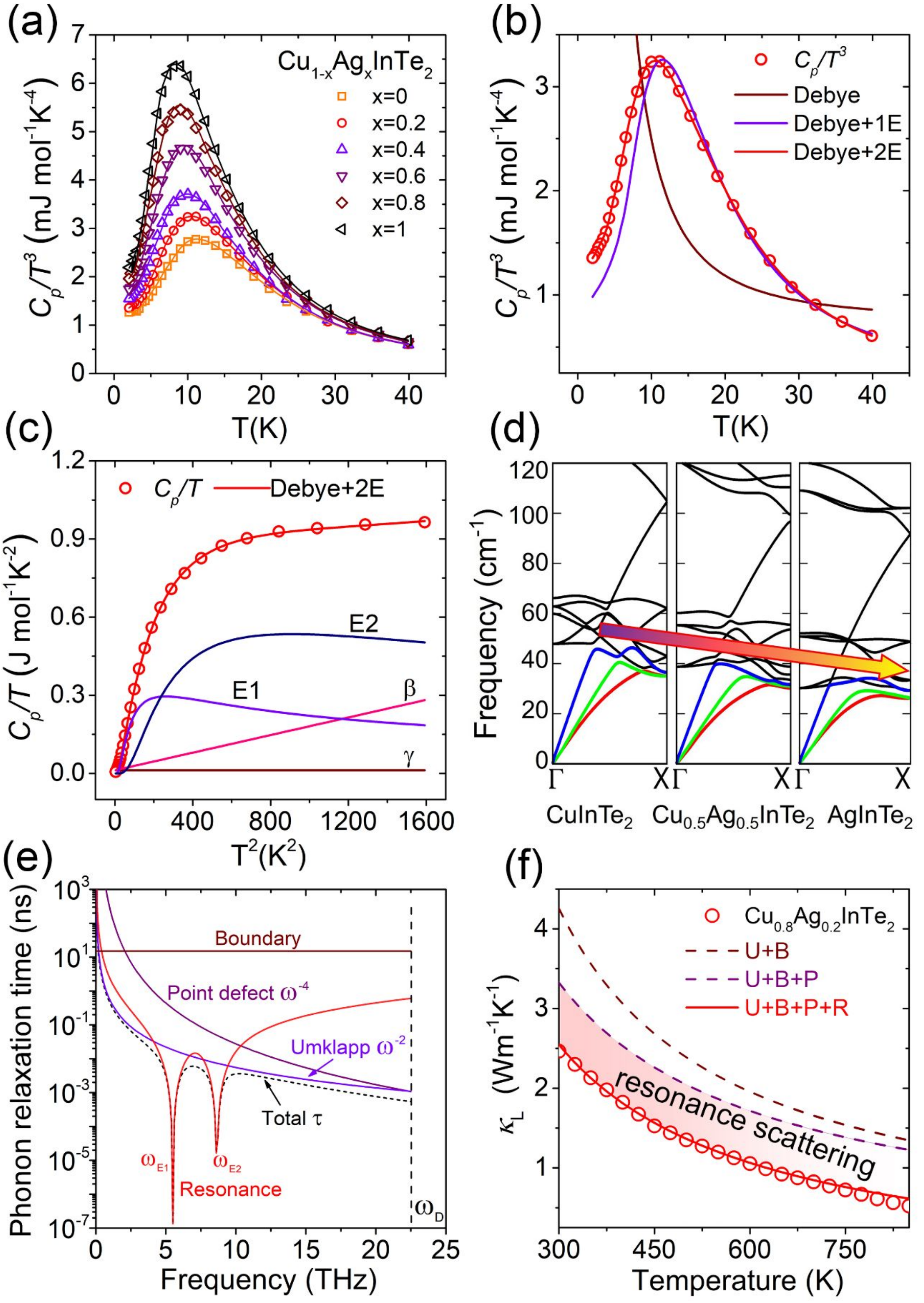

Figure 9. (a) The relationship between C_p/T^3 and T for $Cu_{1-x}Ag_xInTe_2$ (x = 0, 0.2, 0.4, 0.6, 0.8 and 1). The Boson peak is observed around 10-15 K for all samples and is enhanced in magnitude with increasing Ag content. (b) The relationship between C_p/T^3 and T for $Cu_{0.8}Ag_{0.2}InTe_2$. Obviously, the Boson peak can be fitted only with the Debye-2Einstein model

rather than the Debye model and Debye-1Einstein model. (c) C_p/T as a function of T^2 for $Cu_{0.8}Ag_{0.2}InTe_2$. The red solid line is calculated using the Debye-2Einstein model. The individual contributions from electronic (γ), Debye (β), and the two Einstein terms (E1, E2) are also plotted. (d) The comparison of phonon dispersions between $CuInTe_2$, $Cu_{0.5}Ag_{0.5}InTe_2$ and $AgInTe_2$ along ΓX. (e) Calculated phonon relaxation times τ versus phonon frequency ω for $Cu_{0.8}Ag_{0.2}InTe_2$ with different scattering mechanisms. (f) Contribution of various scattering processes to the lattice thermal conductivity of $Cu_{0.8}Ag_{0.2}InTe_2$; here the U, B, P and R represent Umklapp scattering, grain boundaries scattering, point defect scattering, and phonon resonance scattering, respectively.

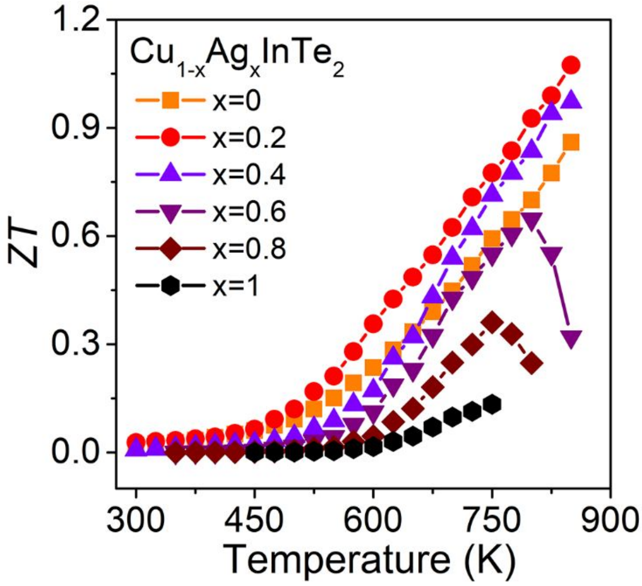

Figure 10. The temperature dependence of the figure of merit *ZT* for $Cu_{1-x}Ag_xInTe_2$ (x = 0, 0.2, 0.4, 0.6, 0.8 and 1).

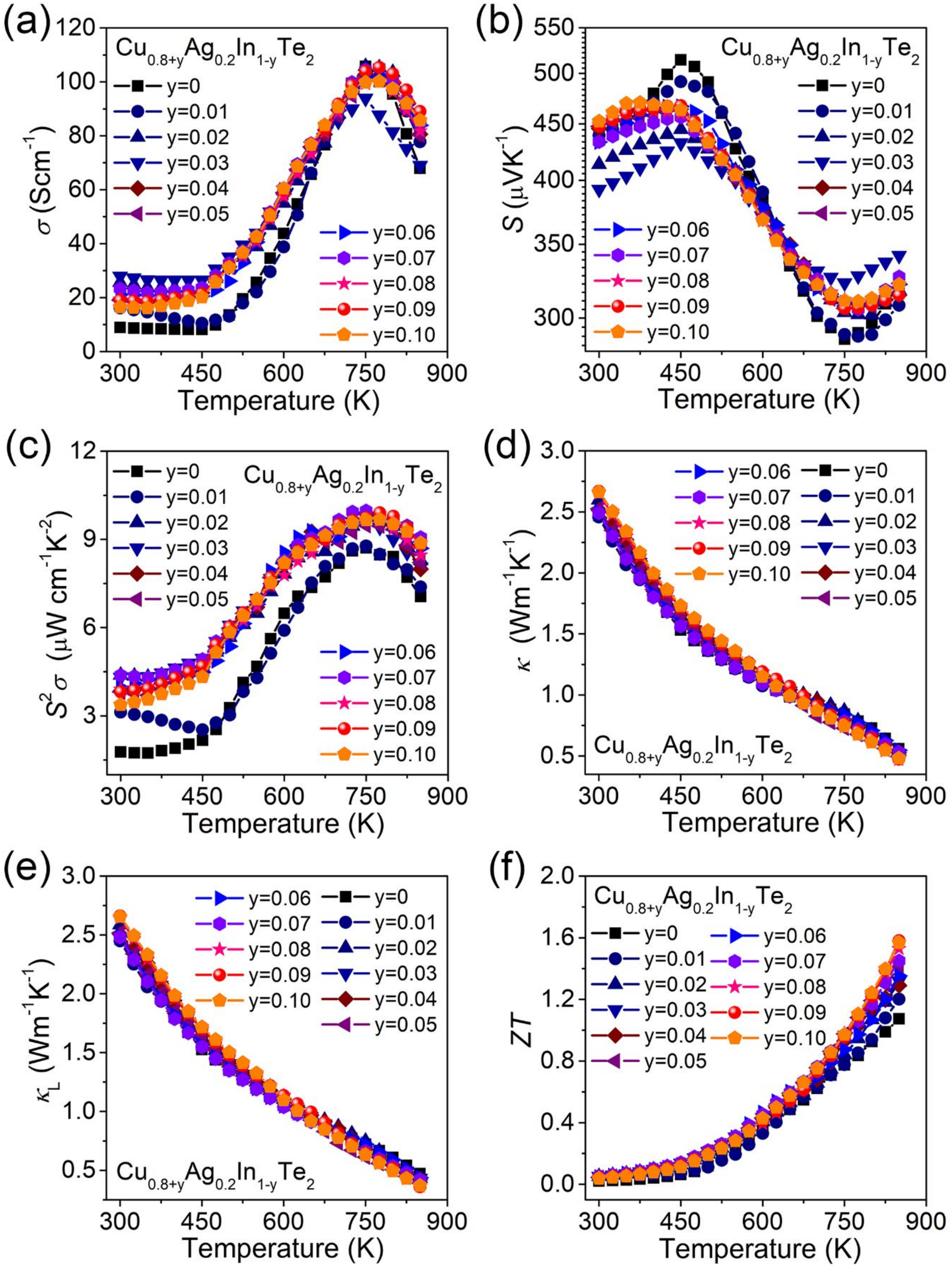

Figure 11. The temperature dependence of (a) the electrical conductivity, (b) the Seebeck coefficients, (c) the power factor, (d) the total thermal conductivity, (e) the lattice thermal conductivity and (f) the figure of merit *ZT* for $Cu_{0.8+y}Ag_{0.2}In_{1-y}Te_2$ (y = 0, 0.01, 0.02, 0.03, 0.04, 0.05, 0.06, 0.07, 0.08, 0.09 and 0.10).

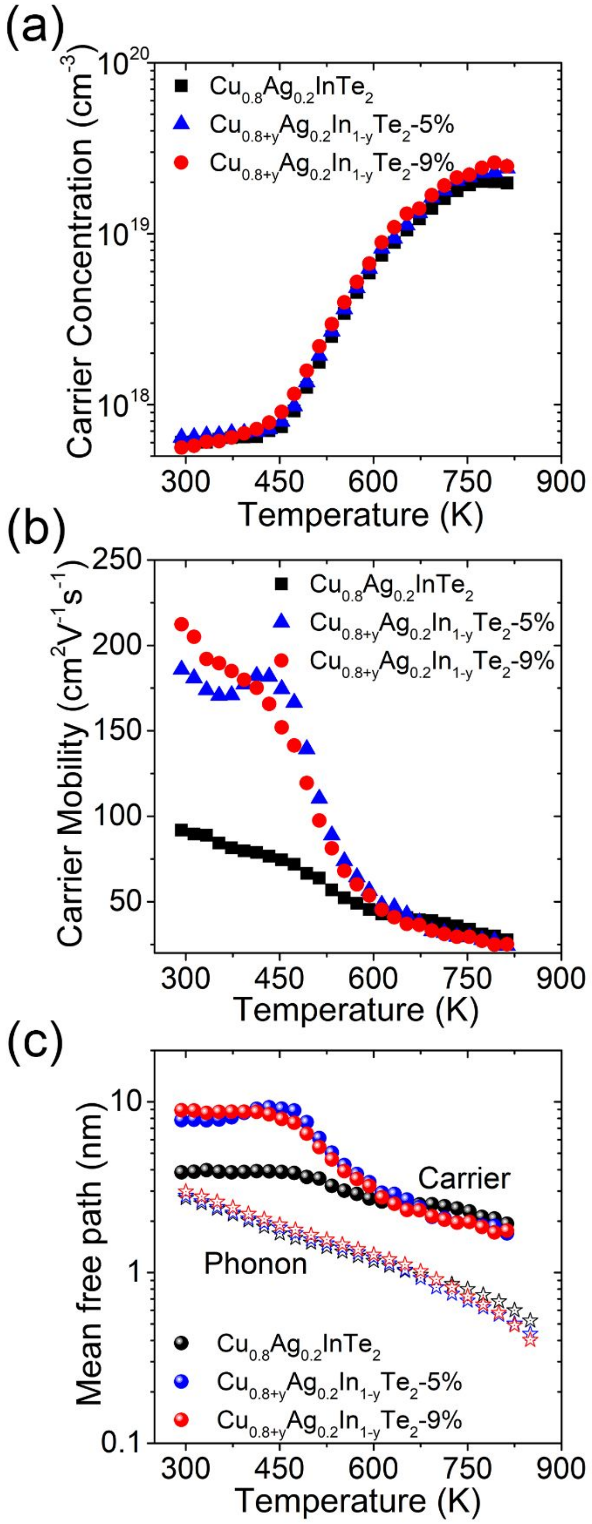

Figure 12. The temperature dependence of (a) carrier concentration, (b) carrier mobility and (c) phonon mean free path and carrier mean free path for $Cu_{0.8}Ag_{0.2}InTe_2$, $Cu_{0.85}Ag_{0.2}In_{0.95}Te_2$ (5%Cu) and $Cu_{0.89}Ag_{0.2}In_{0.91}Te_2$ (9%Cu).

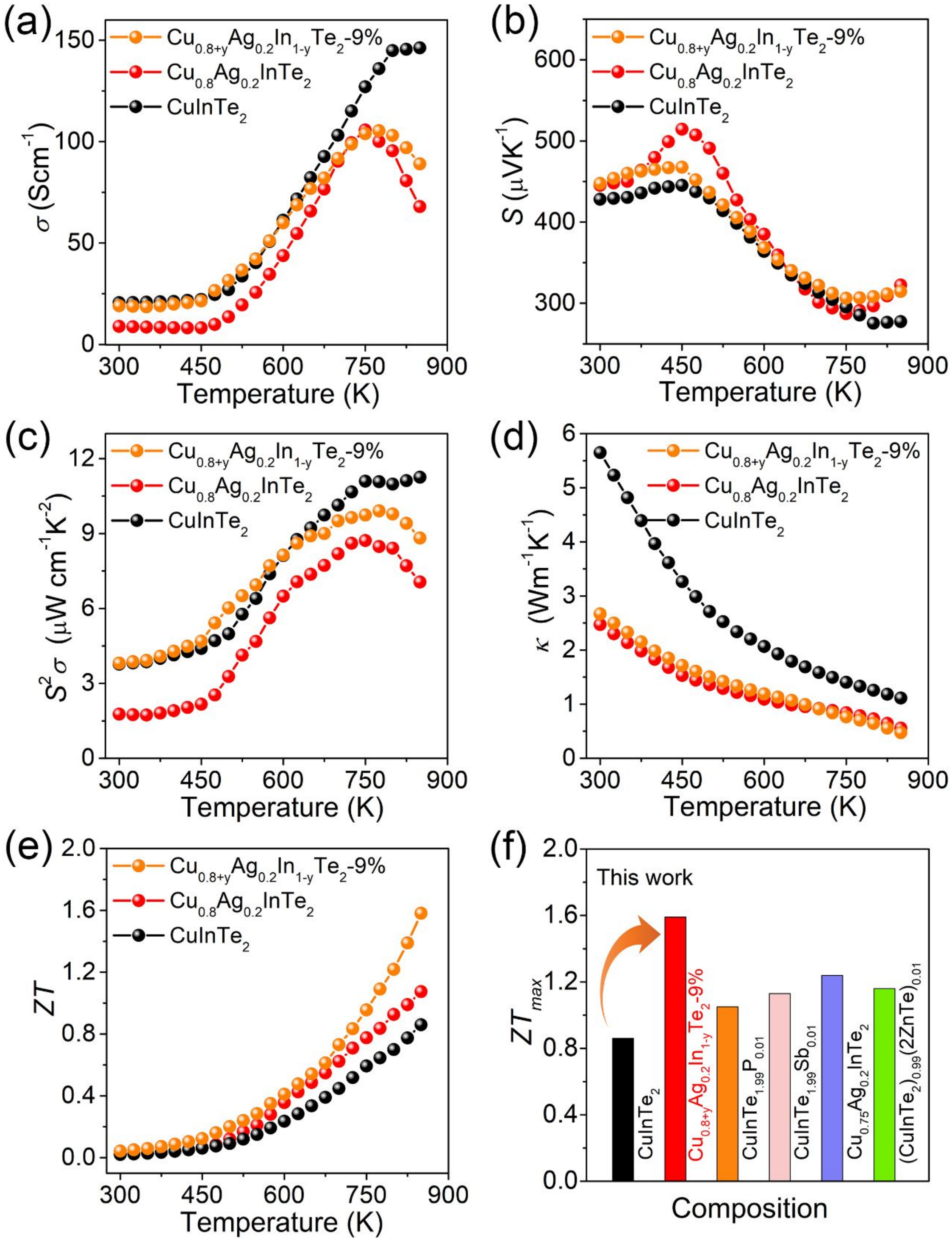

Figure 13. The temperature dependence of (a) the electrical conductivity, (b) the Seebeck coefficients, (c) the power factor, (d) the lattice thermal conductivity and (e) the figure of merit *ZT* for $CuInTe_2$, $Cu_{0.8}Ag_{0.2}InTe_2$ and $Cu_{0.89}Ag_{0.2}In_{0.91}Te_2$. (f) A comparison of maximum *ZT* for $CuInTe_2$-based TE materials.

Table 1. Room temperature physical parameters of $Cu_{1-x}Ag_xInTe_2$ (x = 0, 0.2, 0.4, 0.6, 0.8 and 1). Here, E_g is the electronic energy band gap, κ_L is lattice thermal conductivity, σ is electrical conductivity, p_H is carrier concentration, μ_H is the carrier mobility, and $S_{(450K)}$ represents the Seebeck coefficient at 450 K.

Samples	Chemical Composition	E_g (eV)	κ_L ($Wm^{-1}K^{-1}$)	σ (10^2Scm^{-1})	$S_{(450K)}$ (μVK^{-1})	p_H (cm^{-3})	μ_H ($cm^2V^{-1}s^{-1}$)
$CuInTe_2$	$Cu_{24.50}In_{25.76}Te_{49.74}$	0.93	5.64	0.21	445	1.25×10^{18}	103.1
$Cu_{0.8}Ag_{0.2}InTe_2$	$Cu1_{9.60}Ag_{5.31}In_{25.31}Te_{49.78}$	0.92	2.46	0.08	514	5.58×10^{17}	90.7
$Cu_{0.6}Ag_{0.4}InTe_2$	$Cu_{14.72}Ag_{10.61}In_{25.53}Te_{49.14}$	0.91	1.88	0.03	556	2.11×10^{17}	74.2
$Cu_{0.4}Ag_{0.6}InTe_2$	$Cu_{9.80}Ag_{16.12}In_{25.10}Te_{48.98}$	0.91	1.58	4.49×10^{-5}	763	1.57×10^{15}	17.9
$Cu_{0.2}Ag_{0.8}InTe_2$	$Cu_{4.93}Ag_{21.81}In_{24.13}Te_{49.13}$	0.93	1.28	1.69×10^{-6}	836	1.03×10^{14}	10.2
$AgInTe_2$	$Ag_{26.40}In_{25.45}Te_{48.15}$	0.95	1.57	6.58×10^{-8}	966	\	\

Table 2. Parameters obtained by fitting the experimental low-temperature heat capacity data to the Debye-Einstein model for $Cu_{1-x}Ag_xInTe_2$ (x = 0, 0.2, 0.4, 0.6, 0.8 and 1). Here, γ is the Sommerfeld constant, b is the Debye lattice term, A_i and θ_{Ei} are the amplitude and the Einstein temperature of the i^{th} Einstein oscillator mode, and θ_D is the Debye temperature.

Samples	γ ($mJmol^{-1}K^{-2}$)	b ($mJmol^{-1}K^{-4}$)	A_1	θ_{E1} (K)	A_2	θ_{E2} (K)	θ_D (K)
$CuInTe_2$	4.11	1.38	1.88	41.36	17.16	69.07	178
$Cu_{0.8}Ag_{0.2}InTe_2$	4.69	1.53	3.14	41.64	13.69	65.58	172
$Cu_{0.6}Ag_{0.4}InTe_2$	6.09	1.86	4.72	42.09	9.01	64.78	161
$Cu_{0.4}Ag_{0.6}InTe_2$	6.22	2.19	4.22	39.37	9.11	54.73	153
$Cu_{0.2}Ag_{0.8}InTe_2$	8.07	2.72	2.60	39.83	7.60	43.79	142
$AgInTe_2$	8.61	3.16	3.58	39.14	7.23	42.53	135

Table 3. Room temperature physical parameters of $Cu_{1-x}Ag_xInTe_2$ (x = 0, 0.2, 0.4, 0.6, 0.8 and 1). Here, κ_L is the lattice thermal conductivity, v_l, v_s and v_{ave} are the measured longitudinal, shear, and averaged sound velocity, respectively, l_{ph} is the phonon mean free path and γ_G is the Grüneisen parameter.

Samples	κ_L ($Wm^{-1}K^{-1}$)	v_l (ms^{-1})	v_s (ms^{-1})	v_{ave} (ms^{-1})	l_{ph} (Å)	γ_G
$CuInTe_2$	5.64	3516	1853	2072	58.91	1.82
$Cu_{0.8}Ag_{0.2}InTe_2$	2.46	3421	1783	1995	27.26	1.86
$Cu_{0.6}Ag_{0.4}InTe_2$	1.88	3414	1702	1909	22.15	2.01
$Cu_{0.4}Ag_{0.6}InTe_2$	1.58	3395	1634	1837	19.80	2.12
$Cu_{0.2}Ag_{0.8}InTe_2$	1.28	3252	1570	1765	17.04	2.12
$AgInTe_2$	1.57	3125	1504	1691	22.27	2.13